External forcing explains recent decadal variability of the ocean carbon sink

Galen McKinley[1,1], Amanda Fay[2,2], Yassir Eddebbar[3,3], Lucas Gloege[2,2], and Nicole Lovenduski[4,4]

[1]Columbia
[2]Columbia University
[3]Scripps / UCSD
[4]University of Colorado

November 30, 2022

Abstract

The ocean has absorbed the equivalent of 39% of industrial-age fossil carbon emissions, significantly modulating the growth rate of atmospheric CO2 and its associated impacts on climate. Despite the importance of the ocean carbon sink to climate, our understanding of the causes of its interannual-to-decadal variability remains limited. This hinders our ability to attribute its past behavior and project its future. A key period of interest is the 1990s, when the ocean carbon sink did not grow as expected. Previous explanations of this behavior have focused on variability internal to the ocean or associated with coupled atmosphere/ocean modes. Here, we use an idealized upper ocean box model to illustrate that two external forcings are sufficient to explain the pattern and magnitude of sink variability since the mid-1980s. First, the global-scale reduction in the decadal-average ocean carbon sink in the 1990s is attributable to the slowed growth rate of atmospheric pCO2. The acceleration of atmospheric pCO2 growth after 2001 drove recovery of the sink. Second, the global sea surface temperature response to the 1991 eruption of Mt Pinatubo explains the timing of the global sink within the 1990s. These results are consistent with previous experiments using ocean hindcast models with and without forcing from variable atmospheric pCO2 and climate variability. The fact that variability in the growth rate of atmospheric pCO2 directly imprints on the ocean sink implies that there will be an immediate reduction in ocean carbon uptake as atmospheric pCO2 responds to cuts in anthropogenic emissions.

External forcing explains recent decadal variability of the ocean carbon sink

Galen A. McKinley[1], Amanda R. Fay[1], Yassir A. Eddebbar[2], Lucas Gloege[1],
Nicole S. Lovenduski[3]

Affiliations: [1] Lamont Doherty Earth Observatory / Columbia University, Palisades NY. [2]Scripps Institution of Oceanography, La Jolla, CA. [3] University of Colorado Boulder, Boulder, CO.
*Corresponding author: Email: mckinley@ldeo.columbia.edu

Key points:

- The reduced ocean carbon sink in the decade of the 1990s can be explained by the slowed growth rate of atmospheric CO_2.
- The global sea surface temperature response to Mt Pinatubo in 1991 explains the intra-decadal pattern of the ocean carbon sink in the 1990s.
- There will be an immediate reduction in ocean carbon uptake as atmospheric pCO_2 responds to cuts in anthropogenic emissions.

The ocean has absorbed the equivalent of 39% of industrial-age fossil carbon emissions, significantly modulating the growth rate of atmospheric CO_2 and its associated impacts on climate. Despite the importance of the ocean carbon sink to climate, our understanding of the causes of its interannual-to-decadal variability remains limited. This hinders our ability to attribute its past behavior and project its future. A key period of interest is the 1990s, when the ocean carbon sink did not grow as expected. Previous explanations of this behavior have focused on variability internal to the ocean or associated with coupled atmosphere/ocean modes. Here, we use an idealized upper ocean box model to illustrate that two external forcings are sufficient to explain the pattern and magnitude of sink variability since the mid-1980s. First, the global-scale reduction in the decadal-average ocean carbon sink in the 1990s is attributable to the slowed growth rate of atmospheric pCO_2. The acceleration of atmospheric pCO_2 growth after 2001 drove recovery of the sink. Second, the global sea surface temperature response to the 1991 eruption of Mt Pinatubo explains the timing of the global sink within the 1990s. These results are consistent with previous experiments using ocean hindcast models with and without forcing from variable atmospheric pCO_2 and climate variability. The fact that variability in the growth rate of atmospheric pCO_2 directly imprints on the ocean sink implies that there will be an immediate reduction in ocean carbon uptake as atmospheric pCO_2 responds to cuts in anthropogenic emissions.

Plain Language Summary

Humans have added 440Pg of fossil fuel carbon to the atmosphere since 1750, driving up the atmospheric CO_2 concentration. But not all of this carbon remains in the atmosphere. The ocean has absorbed 39%, substantially mitigating anthropogenic climate change. Though this "ocean carbon sink" is a critical climate process, our understanding of its mechanisms remains limited. Of great interest is the unexplained slow-down of the ocean carbon sink in the 1990s and a subsequent recovery. In this work, we use a simple globally-averaged model to show that two processes external to the ocean are sufficient to explain the slowing of the ocean carbon sink in the 1990s. First, a reduced rate of accumulation of carbon in the atmosphere after 1989 reduced the atmosphere-ocean gradient that drives the ocean sink. Second, the eruption of Mt Pinatubo led to changes in ocean temperature that modified the timing of the sink from 1991 to 2001. We illustrate that the most important control on the decade-averaged magnitude of the ocean sink is variability in the growth rate of atmospheric CO_2. This implies that as future fossil fuel emission cuts drive reduced growth of atmospheric CO_2, the ocean sink will immediately slow down.

1. Introduction

The ocean has absorbed the equivalent of 39% of fossil carbon emissions since 1750, significantly modulating the growth of atmospheric CO_2 and the associated climate change (Friedlingstein et al. 2019; Le Quéré et al., 2018a,b; McKinley et al., 2017; Ciais et al., 2013). This sink is expected to grow and substantially mitigate atmospheric carbon accumulation for the next several centuries (Randerson et al., 2015). Yet, we lack a detailed understanding of spatial and temporal variability in the sink and its underlying mechanisms. Incomplete understanding of ocean flux variability contributes to significant uncertainty in the global anthropogenic carbon budget for recent decades; this uncertainty is equivalent to ~10% of the atmospheric pCO_2 growth rate (Friedlingstein et al. 2019; Le Quéré et al., 2018a,b). This imbalance, in turn, limits the scientific community's ability to inform international efforts to curb fossil fuel emissions (Peters et al., 2017).

Recent studies have concluded that ocean hindcast models, which have long been used to assess the ocean sink, may significantly underestimate its variability (Gruber et al., 2019a; Le Quéré et al., 2018b). These conclusions are based on comparisons to new observation-based gap-filled products that suggest substantially larger interannual to decadal variability (Landschützer et al., 2015, 2016; Rödenbeck et al., 2013, 2015). It is possible, however, that these gap-filled products do not accurately represent the surface ocean carbon cycle given that their raw input data cover only 1.5% of the global ocean in the last 3 decades, and only 3.5% in the most recent years (Bakker et al., 2016). Variability may be amplified by the significant extrapolation that occurs when global full-coverage maps are produced from these very sparse data (Fay et al., 2018; Rödenbeck et al., 2015).

The ocean carbon sink of the 1990s is of particular interest. During this time, the growth of the ocean sink stalled from its expected growth (DeVries et al., 2019; Fay and McKinley, 2013; Landschützer et al., 2015; Le Quéré et al., 2007; Lovenduski et al., 2008). Using a data-constrained ocean circulation model, it has been suggested that this slow-down was caused by excess outgassing of natural carbon due to an anomalously strong overturning of the ocean's upper 1000m (DeVries et al., 2017). Changing patterns of wind-driven circulation in the Southern Ocean have also been proposed (Gruber et al., 2019a; Landschützer et al., 2015). Consensus has yet to be achieved on the mechanisms driving changes in the 1990s sink. It is critical that we accurately quantify and diagnose this variability so that we can better project the future ocean carbon sink and, thus, the degree to which the ocean carbon sink will continue to mitigate global climate change.

2. Methods

In this study, we compare the ocean carbon sink since 1980 as estimated from six ocean hindcast models, four observationally-based products, and a theoretical upper ocean box model. We supplement our analysis with results from nine ocean hindcast models run in constant climate model (DeVries et al., 2019). Supporting information provides additional methodological details.

2.1 Models and Products

Six (6) ocean hindcast models for 1980-2017 are the primary basis for this analysis (Table S1). Ocean hindcast models are gridded, three dimensional representations of the evolution of the ocean state for recent decades. These models have been forced at the surface by winds, heat and buoyancy fluxes from reanalyses of the past atmospheric state. The models we analyze are those used in the recent versions of the Global Carbon Budget (Le Quéré et al., 2018a,b).

Four (4) observationally-based products are also utilized, chosen because they all cover 1985-2016 (Table S2). While models have full coverage in space and time, in situ observations only cover a small fraction of the global surface ocean. These observation-based products utilize gap-filling techniques to estimate values in all periods and areas not directly observed. Interpolation methods fill spatial and temporal gaps by assuming statistical relationships with neighboring or similar areas with available observations.

Ensemble means of the 4 observationally-based products and the 6 hindcast models are calculated.

2.2 Flux analysis

Model fluxes span years 1980-2017, while observationally-based products span the 1985-2016 period (Table S1, S2). An area-weighted annual mean timeseries is calculated for each model and product for regions of interest: i) global, ii) east equatorial Pacific biome (Fay & McKinley, 2014), and iii) global, excluding east equatorial Pacific biome. We note that individual models and products utilize different methods for the flux calculation, including wind speed products and parameterizations. The standard approach of our field is to use the mean of these estimates as the current best-estimate of the air-sea flux (DeVries et al., 2019; Le Quéré et al., 2018a,b).

2.3 pCO_2 analysis

For pCO_2, hindcast models span 1980-2017, while observationally-based products cover 1985-2016. Detrended pCO_2^{ocean} is obtained by removing the atmospheric trend of 1.70 μatm/yr (the observed average annual atmospheric pCO_2 change for 1980 to 2017) from each time series. ΔpCO_2 is calculated at annual timescales by surface ocean pCO_2 - atmospheric pCO_2 [$\Delta pCO_2 = pCO_2^{ocean} - pCO_2^{atmosphere}$].

2.4 Accounting for open ocean areas without observationally-based estimates

There are large differences in the spatial extent of the observationally-based products compared to the hindcast models. This difference, when left unaccounted for, results in significant discrepancies between models and products for both global mean flux and global mean pCO_2. We correct for spatial coverage differences by calculating the mean flux or mean pCO_2 in the area of each model where there is no coverage for a specific data product. By calculating this offset from 6 models for each individual data-product's spatial coverage, we generate a product-specific offset for the annual time series that corrects for the difference in spatial coverage. As expected, observationally-based products with more complete spatial coverage have smaller offsets (Table S2). The only exception to this data-product correction process is the JENA product (Rödenbeck et al., 2013) because it is produced with full spatial coverage and is primarily used in this analysis on its coarser native grid.

2.5 Upper Ocean Box Model

The box model (Fig S1) solves for the time change of Dissolved Inorganic Carbon (DIC) in single upper ocean box (Equation 1).

$$\frac{\mathrm{dDIC}}{\mathrm{dt}} = \frac{\nu}{\mathrm{V}}\left(\mathrm{DIC_{deep}} - \mathrm{DIC}\right) - \frac{\mathrm{k_w} S_o \rho}{\mathrm{dz}}\left(\mathrm{pCO_2^{ocean}} - \mathrm{pCO_2^{atmosphere}}\right) \qquad (1)$$

The first term on the right of Equation 1 is the overturning circulation (ν) acting on the surface to depth gradient of DIC. V is the volume of the global ocean box, V = A*dz. Our value for the global area removes ice-covered regions. The second term on the right of Equation 1 is the air-sea exchange of CO_2. The rate of flux is set by a piston velocity (k_w), solubility (S_o) and density (ρ) over the depth of the box (dz = 200m), multiplied by the ocean to atmosphere difference of pCO_2 (Wanninkhof, 2014). S_o and pCO_2^{ocean} are calculated using full carbon chemistry (Dickson and Millero, 1987; Mehrbach et al., 1973) given inputs of temperature, salinity, alkalinity and DIC. Parameters choices are globally representative values outside the tropics (Table S3). Consistent with current understanding of the drivers of ocean uptake of anthropogenic carbon (Gruber et al., 2019b), the biological pump is assumed constant over time. This leads to our abiotic formulation. Thus, we remove from the DIC_{deep} concentration the amount of carbon that would be vertically supplied, and then removed biologically. We take a global mean DIC_{deep} concentration of 2320 mmol/m^3 and a biological pump component of this of 265 mmol/m^3 (Sarmiento and Gruber 2006, Table 8.2, Figure 8.4.2, organic + carbonate) leading to DIC_{deep} = 2055 mmol/m^3.

NOAA ESRL surface marine boundary layer annual mean observed $xCO_2^{atmosphere}$ is used to force the model. This is the same $xCO_2^{atmosphere}$ data used to force the ocean hindcast models and observationally-based products, and in conversion to $pCO_2^{atmosphere}$, the water vapor correction is applied. $pCO_2^{atmosphere}$ is interpolated linearly to monthly resolution, using the annual mean value at the mid-point of each year. Temperature is held at a constant global surface ocean value, except if the impact of volcanoes is included (Fig. S2). This estimate of the forced sea surface temperature (SST) response to the El Chichon and Mt Pinatubo volcanic eruptions is based on the Community Earth System Model Large Ensemble (CESM LENS) (Eddebbar et al., 2019). The global-mean expression of this forced temperature anomaly extends to several hundred meters depth in CESM LENS. The box model is time stepped with monthly resolution for 1959-2018. In all cases, the box model is spun up from 1959-1979 using observed $pCO_2^{atmosphere}$ and the values presented in Table S3.

The mean uptake flux in the box model is most sensitive to the depth of the box and the global overturning rate (Fig S3, Supporting Information). We use dz = 200m and set other parameters to result in a mean flux and ΔpCO_2 consistent with the ocean models and observationally-based products.

3. Results/Discussion

Global air-sea CO_2 flux variability estimated by the ensemble means of ocean hindcast models and of observationally-based products (Gruber et al., 2019a; Landschützer et al., 2016) are highly correlated (r = 0.95) (Fig 1a, Table S4). The decadal variability of the air-sea CO_2 flux is not driven by a single region, but instead is largely globally coherent (DeVries et al., 2019; Le Quéré et al., 2018b). This air-sea CO_2 flux is primarily determined by the difference of the surface ocean and

the atmosphere pCO_2, $\Delta pCO_2 = pCO_2^{ocean} - pCO_2^{atmosphere}$ (Fay & McKinley, 2013; Landschützer et al., 2015; Lovenduski et al., 2007; McKinley et al., 2017) with a more negative ΔpCO_2 driving a greater ocean uptake. From 1991 to 1993, ΔpCO_2 experiences a negative or neutral anomaly on the global average and at most latitudes over the 91% of ocean that is south of 45°N (Fig 2, S3). From 1993-1995 and again for 1999-2001, ΔpCO_2 anomalies were positive at most latitudes. In 1997-1998, the El Niño event drove negative ΔpCO_2 anomalies in the tropics (Fig 2), but the El Niño-Southern Oscillation (ENSO) cycle does not dominate the global mean decadal variability (Fig 2, Fig S5). Following 2001, ΔpCO_2 anomalies become much more negative at all latitudes outside the tropics and in the global average (Fig 2).

From 1980 to 2017, $pCO_2^{atmosphere}$ increased from 330 µatm to 394 µatm, and pCO_2^{ocean} follows the atmosphere on the long-term (Fig 3a). Detrending reveals the detailed features of these timeseries (Fig 3b). Growth of $pCO_2^{atmosphere}$ slowed significantly with respect to the long-term trend starting in the late 1980s (Fig 3b, Sarmiento 1993). This change was due in part to a pause of growth in fossil fuel emissions from 1989 to 1994 when fossil fuel emissions were approximately constant at 6.1 PgC/yr (Friedlingstein et al. 2019; Sarmiento et al., 2010). Increased uptake of carbon by the terrestrial biosphere also contributed significantly to this slow down (Brovkin et al., 2010; Sarmiento et al., 2010; Angert et al., 2004). Though some studies have attributed the increased land carbon sink to temperature and radiation changes caused by Mt. Pinatubo's 1991 eruption, there is not a consensus with respect to the mechanisms on land (Frölicher et al., 2011; Brovkin et al., 2010; Sarmiento et al., 2010; Angert et al., 2004; Lucht et al., 2002).

Deviations in the evolution of pCO_2^{ocean} from the evolution of $pCO_2^{atmosphere}$ drive ΔpCO_2 changes in the observationally-based products and hindcast models (Fig 3c). Since global mean ΔpCO_2 is only ~5 µatm (Fig 3c), anomalies of a few µatm in either $pCO_2^{atmosphere}$ or pCO_2^{ocean} can significantly impact the air-sea CO_2 flux. In 1992, growth of pCO_2^{ocean} abruptly slowed in both the hindcast models and the observationally-based products (Fig 3b) and ΔpCO_2 becomes more negative (Fig 3c). From 1992 through 2001, pCO_2^{ocean} increases more rapidly than $pCO_2^{atmosphere}$, driving a positive change in ΔpCO_2 over this period (Fig 3c). For 2002-2011 and beyond, pCO_2^{ocean} grows more slowly than the strongly accelerating $pCO_2^{atmosphere}$, leading to increasingly negative ΔpCO_2 over 2002-2011 (Fig 3c).

Given that global mean changes in the ocean sink (Fig 1) are found to occur at most latitudes (Fig 2), we hypothesize an important role for external forcing. To explore these drivers, we apply the upper ocean box model (Fig S1). The key processes captured by this model are (1) ventilation to the surface of deep waters with low anthropogenic carbon content, and (2) air-sea gas exchange. First, we ask: Are the changes in the growth rate of $pCO_2^{atmosphere}$ (Fig 3a,b) sufficient to substantially modify the global ocean carbon sink?

To test this, the box model is forced only with changes in the observed $pCO_2^{atmosphere}$. When the growth rate of $pCO_2^{atmosphere}$ slows in the late 1980s, growth of pCO_2^{ocean} gradually slows in response (Fig 3b, red dashed line). pCO_2^{ocean} achieves a few years after the $pCO_2^{atmosphere}$ minimum in 1994, consistent with the long equilibration timescale for carbon due to carbonate chemistry (Fig S6). Considering the temporal evolution of the ΔpCO_2 (Fig 3c) and flux over 1988-1994, the rapid slowdown of $pCO_2^{atmosphere}$ growth would have caused an outgassing pulse centered on 1993

(Fig 1b). Beyond 1994, $pCO_2^{atmosphere}$ growth returned to approximately its long-term growth rate and then grew more rapidly after 2001 (Fig 3b). Since pCO_2^{ocean} lags behind $pCO_2^{atmosphere}$, ΔpCO_2 grows more negative as the atmosphere accelerates (Fig 3b,c). For the box model forced only with $pCO_2^{atmosphere}$, this increasingly negative ΔpCO_2 drove a steady increase in ocean uptake from 1994 onward (Fig 1b).

This same response of the global mean air-sea CO_2 flux to $pCO_2^{atmosphere}$ forcing occurs in two types of three-dimensional ocean models with constant circulation. Both an ensemble of ocean hindcast models with constant climate forcing (DeVries et al., 2019) and the data-constrained constant circulation Ocean Circulation Inverse Model (OCIM) (DeVries, 2014) have the same flux response as in the box model forced only with variable $pCO_2^{atmosphere}$ (Fig 1b). Correlations across these models are almost perfect (r=0.97-0.98, dashed lines in Fig 1b) and remain very high even when independently detrended (r>0.91, Table S4). This correspondence emphasizes the critical role of variability in the growth of $pCO_2^{atmosphere}$ to variability in the ocean sink. It also serves as evidence that the box model is realistically estimating the timing and magnitude of this response.

Though it is the slowed growth of $pCO_2^{atmosphere}$ in the early 1990s that causes the mean 1990s sink to be only 0.1 PgC/yr larger than the sink of the 1980s (Table S5), the pattern of the sink change in the 1990s is clearly inconsistent with ocean hindcast models with variable climate (compare bold green to red dash in Fig 1b), and thus is also inconsistent with the observationally-based products (Fig 1a). An additional mechanism is required.

Volcanic eruptions of El Chichon in 1982 and Mt. Pinatubo in 1991 injected large quantities of sulfate aerosols into the stratosphere and dramatically altered global air and sea surface temperatures (Church et al., 2005). The forced response to these eruptions was a substantial oceanic uptake of carbon and oxygen for the following 2-3 years (Eddebbar et al., 2019). Modern earth system models indicate that a significant negative anomaly in global sea surface temperatures (SST) was driven by the eruptions (Eddebbar et al., 2019). For the diagnostic box model, we apply the same magnitude of forced global SST cooling estimated by these models, 0.1^{o}C in 1982 and 0.2^{o}C in 1991 (Fig S2) to evaluate the impact on ocean carbon sink variability.

With this volcano-forced SST variability applied to the box model, strong coolings in 1982 and in 1991 drive a rapid drop of pCO_2^{ocean} (Fig 3b, solid red) and a strong uptake anomaly (Fig 1, red bold). The reduced flux that would have occurred in the early 1990s due to the slowing of $pCO_2^{atmosphere}$ (Fig 1b, red dash) was overwhelmed by the rapid cooling due to Mt. Pinatubo and thus, a strong uptake pulse occurred (Fig 1b, red bold). The re-warming and excess DIC in the surface ocean that follow Mt. Pinatubo elevates pCO_2^{ocean} relative to $pCO_2^{atmosphere}$ through 2001, leading to ΔpCO_2 becoming less negative over this period (Fig 3c). Thus, the sink stagnates from the early to late 1990s (Fig 1). The net effect of both forcings is that the reduced sink of the early 1990s caused by the slowed $pCO_2^{atmosphere}$ growth rate is shifted to the late 1990s by the rapid cooling and slow re-warming caused by Mt. Pinatubo. In summary, the climate variability mechanism that led to a neutral 1990s intra-decadal trend of the ocean carbon sink (DeVries et al. 2019) contains a major contribution from the ocean's response and recovery from Pinatubo cooling, i.e. a response to external forcing from volcanos.

CO_2 fluxes from the diagnostic box model forced with both observed $pCO_2^{atmosphere}$ and the volcanoes' impacts on sea surface temperature are highly correlated to the ensemble mean of the observationally-based products for their overlapping periods (r = 0.89, 1985-2016) and hindcast models (r=0.92, 1980-2017) (Fig 1a, Table S4). The simplicity of these global mechanisms and the strong correspondence of the resulting decadal variability to the products and the models supports the conclusion that global air-sea CO_2 flux variability since 1980 has been significantly driven by external forcing from (1) the changing $pCO_2^{atmosphere}$ growth rate and (2) in the 1990s, the surface ocean temperature effects of Mt. Pinatubo (Fig 4).

Since ocean carbon uptake is enhanced with the eruption of large volcanos, the effect on $pCO_2^{atmosphere}$ would ideally be modeled interactively. Unfortunately, land carbon sink uncertainties preclude this. The sea surface temperature effects of Pinatubo led to an increased ocean sink of approximately 0.5 PgC/yr (Fig.1b), but estimates of the land sink anomaly at this time are much larger and uncertain, ranging 1-2 PgC/yr (Sarmiento et al. 2010; Angert et al. 2004; Sarmiento 1993). In fact, the post-Pinatubo period is one of maximum uncertainty in the post-1960 Global Carbon Budget (Friedlingstein et al. 2019, Peters et al. 2017). Soon after the eruption of Mt. Pinatubo, Sarmiento (1993) noted the coincident slowdown in growth of $pCO_2^{atmosphere}$ and reported that ^{13}C records at that time suggested a terrestrial driver, while O_2/N_2 records suggested an oceanic driver. A modern reconsideration of ^{13}C and O_2/N_2 records may lead to better understanding of this partitioning.

This analysis illustrates that externally forced variability played an important role in recent decadal variability of the ocean carbon sink. However, the total climate variability in any variable is the sum of forced variability caused by drivers external to the system, and internal variability due to system dynamics (Deser et al., 2012). We have recently reviewed the many previous studies on mechanisms of ocean carbon sink variability (McKinley et al., 2017). Processes discussed have included the variable upper ocean circulation, wind and circulation patterns in the Southern Ocean, and modes of coupled atmosphere/ocean variability in both hemispheres (DeVries et al., 2017, 2019; Gruber et al., 2019a; Landschützer et al., 2015, 2019; Lovenduski et al., 2007). These analyses have focused on variability internal to the ocean or associated with coupled atmosphere/ocean modes (McKinley et al., 2017), but have not been able to comprehensively explain the global-scale decadal variability. Here, we illustrate that the observed changes can, to first order, be attributed to two forcings external to the ocean.

Previous studies have also typically focused on a single model or a single observationally-based product. However, for the best estimate of the real ocean's flux variability, it is common practice to use the ensemble mean of ocean models and/or of observationally-based products (Friedlingstein et al. 2019; DeVries et al., 2019; Le Quéré et al., 2018a,b), which is our approach. Only the internal variability that is represented in most ensemble members will be preserved in the ensemble average. Averaging damps internal variability of the individual members and thus amplifies the common forced component (McKinley et al., 2016, 2017; Deser et al., 2012). Our results illustrate that the current best estimate of the real ocean's flux variability, based on this ensemble average, can be explained largely with forced mechanisms. However, because we do not have enough information to determine which member of the ensemble best approximates the ocean's true internal variability, this current best estimate potentially underestimates the full impact of internal variability in the carbon sink of the real ocean.

What is the range of magnitude of internal variability that may be occurring in addition to the forced variability that we identify? Individual observationally-based products have a range of detrended flux variability from 0.14-0.30 PgC/yr, while the ensemble mean variability is 0.19 PgC/yr (1σ for 1985-2016). For the hindcast models, the range is 0.10-0.20 PgC/yr and the ensemble mean variability is 0.11 PgC/yr for the same years. Our estimate of the amplitude of externally-forced variability from the box model is 0.14 PgC/yr (Fig 1). By this measure, externally forced variability as estimated by the box model is approximately equal to the total amplitude common to the hindcast models, but is only about 70% of the variability common to the products. On top of this, the individual models and products suggest a wide range of additional internal variability. In future studies, separation of the forced component of ocean carbon sink variability driven by changing $pCO_2^{atmosphere}$ and volcanos from the total variability in individual models and products should help to clarify the patterns, magnitudes, and physical and biogeochemical mechanisms of internal variability in the real ocean. For diagnostic (Friedlingstein et al. 2019; Le Quéré et al., 2018a,b) and predictive purposes (Randerson et al., 2015) it is critical to also determine which model and observationally-based estimates best represent both the internal and forced variability of the real ocean.

Though our box model is sufficient to represent the global-mean behavior of the externally-forced ocean carbon sink in recent decades, other mechanisms may increase in importance in the future. As climate changes have increased impact on ocean physics and biogeochemistry, feedbacks on the carbon sink of increasing magnitude can be expected. Future reduction in the overturning circulation, or increased re-emergence of waters already carrying a high anthropogenic carbon load would reduce the sink. A weaker biological pump would also damp net ocean carbon uptake (Kwon et al. 2009). The reduced buffer capacity of the surface ocean should grow in importance over time, particularly under high emission scenarios (Fassbender et al. 2017). As mitigation of CO_2 emissions occurs, the growth rate of $pCO_2^{atmosphere}$ will slow. With this reduced external forcing, the imprint of internal variability on the sink should become more evident. Improved understanding of both internal and external mechanisms is essential to continue to accurately diagnose the evolving ocean carbon sink, and to improve model-based predictions.

4. Conclusions

We have shown that externally forced variability is sufficient to explain a significant portion of current model and observationally-based best-estimates of the recent decadal variability of the global ocean carbon sink (Fig 1a). The reduced ocean carbon sink in the decade of the 1990s was driven by a slowed growth rate of $pCO_2^{atmosphere}$. The intra-decadal timing of the slowed growth rate in the 1990s was due to the surface ocean temperature response to the Mt. Pinatubo eruption in 1991. Volcano-driven cooling first led to an anomalously large sink, and then as surface ocean temperatures recovered, pCO_2^{ocean} was elevated causing the sink to slow. In the box model, only this SST response is needed to replicate the behavior of the observationally-based products and the ocean hindcast models (Fig 1), but it would be of great value to perform a deeper analysis of the upper ocean response to Mt. Pinatubo with future studies. From 2001 on, the recovery of the global ocean carbon sink is attributable to the enhanced growth rate of $pCO_2^{atmosphere}$ (Fig 4).

Implications for the future ocean carbon sink are several. First, we note the relative importance of external vs internal drivers of ocean sink change can be expected to change, and thus both must be

understood. Regarding external forcing, future large volcanic eruptions cannot be predicted, and it is difficult to predict the detailed future of $pCO_2^{atmosphere}$. Thus, these are now identified as additional sources of uncertainty in decadal predictions and long-term projections (Lovenduski et al., 2019; McKinley et al., 2017). The timescales on which additional human interventions in the climate system, such as solar radiation management or nuclear conflict, would mimic these externally forced changes and modify the ocean carbon sink should be considered (Lovenduski et al. 2020; Lauvset et al., 2017). Finally, since the changing growth rate of $pCO_2^{atmosphere}$ is the primary driver of recent variability in the ocean carbon sink, the ocean sink should be expected to slow as reductions in the $pCO_2^{atmosphere}$ growth rate occur in response to climate change mitigation efforts (Peters et al., 2017). It is important that this critical feedback on the atmospheric CO_2 content be accurately estimated and accounted for in policy making.

Acknowledgments: Funding from many countries and agencies has supported the collection of surface ocean pCO_2 data, for development of ocean hindcast models and observationally-based products, and for international coordination. Ocean hindcast models with real climate are available from https://www.globalcarbonproject.org/carbonbudget/18/data.htm; ocean hindcast models with constant climate are available from DeVries et al. (2019); and observationally-based products are available from https://www.nodc.noaa.gov/ocads/oceans/SPCO2_1982_2015_ETH_SOM_FFN.html (SOM-FFN), http://www.bgc-jena.mpg.de/CarboScope/ (JENA), https://doi.org/10.6084/m9.figshare.7894976.v1 (CSIR), and http://dods.lsce.ipsl.fr/invsat/CMEMS/ (LSCE). The code for the upper ocean box model is available (https://doi.org/10.6084/m9.figshare.11983947.v1). G.A.M., A.R.F and L.G. were supported by NASA NNX17AK19G and by Columbia University. G.A.M., A.R.F. and N.S.L. were supported by NSF OCE-1948664 and OCE-1558225. N.S.L. was also supported by NSF OCE-1752724, NSF PLR-13009540, and the Open Philanthropy Project. This work would not be possible without the efforts of many scientists who have collected surface ocean pCO_2 data and contributed it to the SOCAT database, and to the developers of the observationally-based products based on these data. We thank also the scientists who have contributed their ocean hindcast model results to the Global Carbon Project. Leadership from the International Ocean Carbon Coordinating Project (IOCCP) and the Global Carbon Project (GCP) has been essential to the success of these efforts.

References

Angert, A., Biraud, S., Bonfils, C., Buermann, W., & Fung, I. (2004). CO2 seasonality indicates origins of post-Pinatubo sink. *Geophysical Research Letters*, *31*(11).

Bakker, D. C. E., Pfeil, B., Landa, C. S., Metzl, N., O'Brien, K. M., Olsen, A., et al. (2016). A multi-decade record of high-quality fCO_2 data in version 3 of the Surface Ocean CO2 Atlas (SOCAT), Earth Syst. Sci. Data, 8, 383–413.

Brovkin, V., Loren, S., Jungclaus, J., Raddatz, T., Timmreck, C., Reick, C., et al. (2010). Sensitivity of a coupled climate-carbon cycle model to large volcanic eruptions during the last millennium. *Tellus B: Chemical and Physical Meteorology*, *62*(5), 674-681.

Buitenhuis, E. T., Rivkin, R. B., Sailley, S., & Le Quéré, C. (2010). Biogeochemical fluxes through microzooplankton. *Global biogeochemical cycles*, *24*(4).

Canadell, J. G., Ciais, P., Gurney, K., Le Quéré, C., Piao, S., Raupach, M. R., & Sabine, C. L. (2011). An international effort to quantify regional carbon fluxes. *Eos, Transactions American Geophysical Union*, *92*(10), 81-82.

Church, J. A., White, N. J., & Arblaster, J. M. (2005). Significant decadal-scale impact of volcanic eruptions on sea level and ocean heat content. *Nature*, *438*(7064), 74.

Ciais, P., Sabine, C., Bala, G., Bopp, L., Brovkin, V., Canadell, J. et al. (2013). The physical science basis. Contribution of working group I to the fifth assessment report of the intergovernmental panel on climate change. *IPCC Climate Change*, 465-570.

Denvil-Sommer, A., Gehlen, M., Vrac, M., & Mejia, C. (2019). LSCE-FFNN-v1: a two-step neural network model for the reconstruction of surface ocean pCO 2 over the global ocean. *Geoscientific Model Development*, *12*(5), 2091-2105.

Deser, C., Phillips, A., Bourdette, V., & Teng, H. (2012). Uncertainty in climate change projections: the role of internal variability. *Climate dynamics*, *38*(3-4), 527-546.

DeVries, T. (2014). The oceanic anthropogenic CO2 sink: Storage, air-sea fluxes, and transports over the industrial era. *Global Biogeochemical Cycles*, *28*(7), 631-647.

DeVries, T., Holzer, M., & Primeau, F. (2017). Recent increase in oceanic carbon uptake driven by weaker upper-ocean overturning. *Nature*, *542*(7640), 215.

DeVries, T., Le Quéré, C., Andrews, O., Berthet, S., Hauck, J., Ilyina, T., et al. (2019). Decadal trends in the ocean carbon sink. *Proceedings of the National Academy of Sciences*, *116*(24), 11646-11651.

Dickson, A. G., & Millero, F. J. (1987). A comparison of the equilibrium constants for the dissociation of carbonic acid in seawater media. *Deep Sea Research Part A. Oceanographic Research Papers*, *34*(10), 1733-1743.

Dickson, A. G., Sabine, C. L., and Christian, J. R. (Eds.): Guide to Best Practices for Ocean CO2 Measurements, PICES Special Publication, IOCCP Report No. 8, 2007. 8825

Dlugokencky, E.J., Thoning, K.W., Lang, P.M., Tans, P.P. (2017) NOAA Greenhouse Gas Reference from Atmospheric Carbon Dioxide Dry Air Mole Fractions from the NOAA ESRL Carbon Cycle Cooperative Global Air Sampling Network.

Doney, S. C., Lima, I., Feely, R. A., Glover, D. M., Lindsay, K., Mahowald, N., et al. (2009). Mechanisms governing interannual variability in upper-ocean inorganic carbon system and air–sea CO2 fluxes: Physical climate and atmospheric dust. *Deep Sea Research Part II: Topical Studies in Oceanography*, *56*(8-10), 640-655.

Eddebbar, Y. A., Rodgers, K. B., Long, M. C., Subramanian, A. C., Xie, S. P., & Keeling, R. F. (2019). El Niño–Like Physical and Biogeochemical Ocean Response to Tropical Eruptions. *Journal of Climate*, *32*(9), 2627-2649.

Fassbender, A. J., Sabine, C. L., & Palevsky, H. I. (2017). Nonuniform ocean acidification and attenuation of the ocean carbon sink. Geophysical Research Letters, 44(16), 8404–8413.

Fay, A. R., & McKinley, G. A. (2013). Global trends in surface ocean pCO2 from in situ data. *Global Biogeochemical Cycles*, *27*(2), 541-557.

Fay, A. R., & McKinley, G. A. (2014). Global open-ocean biomes: mean and temporal variability. *Earth System Science Data*, *6*(2), 273-284.

Fay, A. R., Lovenduski, N. S., McKinley, G. A., Munro, D. R., Sweeney, C., Gray, A. R., et al. (2018). Utilizing the Drake Passage Time-series to understand variability and change in subpolar Southern Ocean pCO2. *Biogeosciences*, *15*, 3841-3855.

Friedlingstein, P., Jones, M.W., O'Sullivan, M., Andrew, R.M, Hauck, J. et al. (2019), Global Carbon Budget 2019, *Earth Syst. Sci. Data*, *11*(4), 1783–1838.

Frölicher, T., Joos, F., & Raible, C. (2011). Sensitivity of atmospheric CO2 and climate to explosive volcanic eruptions. *Biogeosciences*, *8*(8), 2317-2339.

Gregor, L., Lebehot, A.D., Kok, S., Monteiro, P.M.S. (2019) A comparative assessment of the uncertainties of global surface ocean CO_2 estimates using a machine learning ensemble (CSIR-ML6 version 2019a) – have we hit the wall? *Geosci. Model Dev. Discuss.*.

Gruber, N., Gloor, M., Mikaloff Fletcher, S. E., Doney, S. C., Dutkiewicz, S., Follows, M. J., et al. (2009). Oceanic sources, sinks, and transport of atmospheric CO2. *Global Biogeochemical Cycles*, *23*(1).

Gruber, N., Landschützer, P., & Lovenduski, N. S. (2019a). The variable Southern Ocean carbon sink. *Annual review of marine science*, *11*, 159-186.

Gruber, N., Clement, D., Carter, B. R., Feely, R. A., Van Heuven, S., Hoppema, M., et al. (2019b). The oceanic sink for anthropogenic CO2 from 1994 to 2007. *Science*, *363*(6432), 1193-1199.

Hauck, J., Lenton, A., Langlais, C., & Matear, R. (2018). The fate of carbon and nutrients exported out of the Southern Ocean. *Global Biogeochemical Cycles*, *32*(10), 1556-1573.

Jacobson, A. R., Mikaloff Fletcher, S. E., Gruber, N., Sarmiento, J. L. and Gloor M. (2007), A joint atmosphere-ocean inversion for surface fluxes of carbon dioxide: 1. Methods and global-scale fluxes, Global Biogeochem. Cycles, 21, GB1019, doi:10.1029/2005GB002556

Kalnay, E., Kanamitsu, M., Kistler, R., Collins, W., Deaven, D., Gandin, L., et al. (1996). The NCEP/NCAR 40-year reanalysis project. *Bulletin of the American meteorological Society*, *77*(3), 437-472.

Kwon, E. Y., F. Primeau, and J. L. Sarmiento (2009), The impact of remineralization depth on the air-sea carbon balance, *Nature Geoscience*, *2*(9), 630–635, doi:10.1038/NGEO612.

Landschützer, P., Gruber, N., Haumann, F. A., Rödenbeck, C., Bakker, D. C., Van Heuven, S., et al. (2015). The reinvigoration of the Southern Ocean carbon sink. *Science*, *349*(6253), 1221-1224.

Landschützer, P., Gruber, N., & Bakker, D. C. (2016). Decadal variations and trends of the global ocean carbon sink. *Global Biogeochemical Cycles*, *30*(10), 1396-1417.

Landschützer, P., Gruber, N., Bakker, D. C. E., & Landschützer, P. (2017). An updated Observation-Based Global Monthly Gridded Sea Surface pCO2 and Air-sea CO2 Flux Product from 1982 Through 2015 and Its Monthly Climatology. *NCEI Accession*, *160558*.

Landschützer, P., Ilyina, T., & Lovenduski, N. S. (2019). Detecting Regional Modes of Variability in Observation-Based Surface Ocean p CO2. *Geophysical Research Letters*, *46*(5), 2670-2679.

Lauvset, S. K., Tjiputra, J., & Muri, H. (2017). Climate engineering and the ocean: effects on biogeochemistry and primary production. *Biogeosciences*, *14*(24), 5675-5691.

Le Quéré, C., Rödenbeck, C., Buitenhuis, E. T., Conway, T. J., Langenfelds, R., Gomez, A., et al. (2007). Saturation of the Southern Ocean CO_2 sink due to recent climate change. *Science*, *316*(5832), 1735-1738.

Le Quéré, C., Andrew, R. M., Friedlingstein, P., Sitch, S., Pongratz, J., Manning, A. C., et al. (2018). Global carbon budget 2017. *Earth Syst. Sci. Data*, *10*(1), 405-448.

Le Quéré, C., Andrew, R. M., Friedlingstein, P., Sitch, S., Hauck, J., Pongratz, J., et al. (2018). Global carbon budget 2018. *Earth System Science Data (Online)*, *10*(4).

Lovenduski, N. S., Gruber, N., Doney, S. C., & Lima, I. D. (2007). Enhanced CO2 outgassing in the Southern Ocean from a positive phase of the Southern Annular Mode. *Global Biogeochemical Cycles*, *21*(2).

Lovenduski, N. S., Gruber, N., & Doney, S. C. (2008). Toward a mechanistic understanding of the decadal trends in the Southern Ocean carbon sink. *Global Biogeochemical Cycles*, *22*(3).

Lovenduski, N. S., Yeager, S. G., Lindsay, K., & Long, M. C. (2019). Predicting near-term variability in ocean carbon uptake. *Earth System Dynamics*, *10*(1), 45-57.

Lovenduski, N. S., Harrison, C. S. , Olivarez, H., Bardeen, C. G., Toon, O. B., Coupe, J., Robock, A., Rohr, T., and Stevenson S. (2020), The Potential Impact of Nuclear Conflict on Ocean Acidification, *Geophys Res Lett*, *47*(3), 1535, doi:10.1007/s10584-012-0475-8.

Lucht, W., Prentice, I. C., Myneni, R. B., Sitch, S., Friedlingstein, P., Cramer, W et al. (2002). Climatic control of the high-latitude vegetation greening trend and Pinatubo effect. *Science*, *296*(5573), 1687-1689.

McKinley, G. A., Pilcher, D. J., Fay, A. R., Lindsay, K., Long, M. C. and Lovenduski, N. S. (2016), Timescales for detection of trends in the ocean carbon sink, *Nature*, *530*(7591), 469–472.

McKinley, G. A., Fay, A. R., Lovenduski, N. S., & Pilcher, D. J. (2017). Natural variability and anthropogenic trends in the ocean carbon sink. *Annual review of marine science*, *9*, 125-150.

Mehrbach, C., Culberson, C. H., Hawley, J. E., & Pytkowicx, R. M. (1973). Measurement of the apparent dissociation constants of carbonic acid in seawater at atmospheric pressure 1. *Limnology and Oceanography*, *18*(6), 897-907.

Naegler, T., P. Ciais, K. Rodgers, and I. Levin (2006), Excess radiocarbon constraints on air-sea gas exchange and the uptake of CO2 by the oceans, *Geophys Res Lett*, *33*(11), L11802, doi:10.1029/2005GL025408.

Paulsen, H., Ilyina, T., Six, K. D., & Stemmler, I. (2017). Incorporating a prognostic representation of marine nitrogen fixers into the global ocean biogeochemical model HAMOCC. *Journal of Advances in Modeling Earth Systems*, *9*(1), 438-464.

Peters, G. P., Andrew, R. M., Canadell, J. G., Fuss, S., Jackson, R. B., Korsbakken, J. I., et al. (2017). Key indicators to track current progress and future ambition of the Paris Agreement. *Nature Climate Change*, *7*(2), 118.

Randerson, J. T., Lindsay, K., Munoz, E., Fu, W., Moore, J. K., Hoffman, F. M., et al. (2015). Multicentury changes in ocean and land contributions to the climate-carbon feedback. *Global Biogeochemical Cycles*, *29*(6), 744-759.

Reynolds, R. W., Rayner, N. A., Smith, T. M., Stokes, D. C., & Wang, W. (2002). An improved in situ and satellite SST analysis for climate. *Journal of climate*, *15*(13), 1609-1625.

Rödenbeck, C., Keeling, R. F., Bakker, D. C., Metzl, N., Olsen, A., Sabine, C., & Heimann, M. (2013). Global surface-ocean p (CO2) and sea-air CO2 flux variability from an observation-driven ocean mixed-layer scheme.

Rödenbeck, C., Bakker, D. C., Gruber, N., Iida, Y., Jacobson, A. R., Jones, S., et al. (2015). Data-based estimates of the ocean carbon sink variability–first results of the Surface Ocean pCO_2 Mapping intercomparison (SOCOM). *Biogeosciences*, *12*, 7251-7278.

Sarmiento, J. L. (1993), Carbon-Cycle - Atmospheric CO2 Stalled, *Nature*, *365*(6448), 697–698.

Sarmiento, J. L., & Gruber, N. (2006). *Ocean biogeochemical dynamics*. Princeton University Press.

Sarmiento, J. L., Gloor, M., Gruber, N., Beaulieu, C., Jacobson, A. R., Mikaloff Fletcher, S. E., et al. (2010). Trends and regional distributions of land and ocean carbon sinks. *Biogeosciences*, *7*(8), 2351-2367.

Schwinger, J., Goris, N., Tjiputra, J. F., Kriest, I., Bentsen, M., Bethke, I., et al. (2016). Evaluation of NorESM-OC (versions 1 and 1.2), the ocean carbon-cycle stand-alone configuration of the Norwegian Earth System Model (NorESM1). *Geoscientific Model Development*, *9*, 2589-2622.

Séférian, R., Delire, C., Decharme, B., Voldoire, A., y Melia, D. S., Chevallier, M., et al. (2016). Development and evaluation of CNRM Earth system model–CNRM-ESM1.

Takahashi, T., S. Sutherland, R. Wanninkhof, C. Sweeney, R. Feely, D. Chipman, B. Hales, G. Friederich, F. Chavez, and C. Sabine (2009), Climatological mean and decadal change in surface ocean pCO2, and net sea–air CO2 flux over the global oceans, *Deep-Sea Research Part II*, *56*(8-10), 554–577.

Wanninkhof, R. (2014) Relationship between wind speed and gas exchange over the ocean revisited. *Limnology and Oceanography: Methods*, 12(6):351-362.

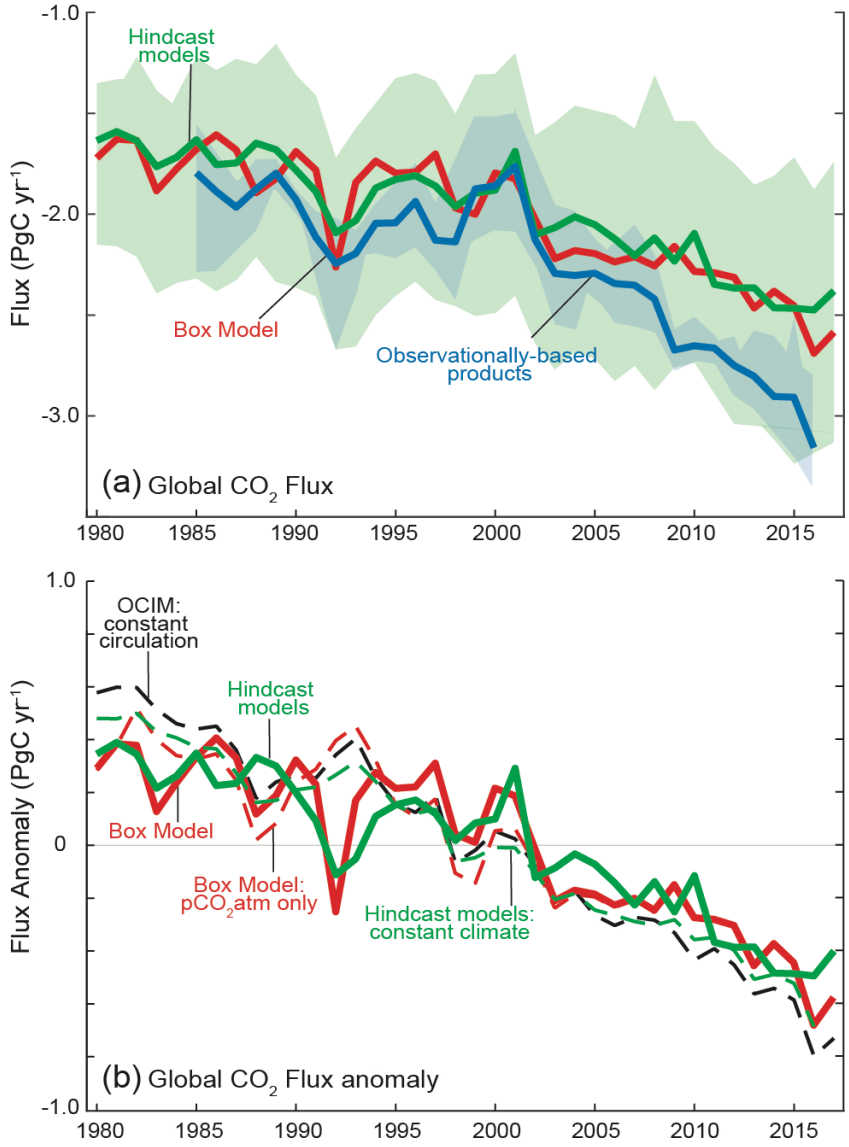

Fig 1: Air-sea CO_2 flux of anthropogenic carbon from observationally-based products (blue), hindcast models (green) and upper ocean diagnostic box model (red); negative flux into the ocean. (**A**) global (bold), with range of individual members (shading), (**B**) anomalies of air-sea CO_2 flux for the hindcast models with constant climate and variable $pCO_2^{atmosphere}$ (green dashed), and variable climate and variable $pCO_2^{atmosphere}$ (solid green); box model with only $pCO_2^{atmosphere}$ forcing (dashed red) and both $pCO_2^{atmosphere}$ and volcano-driven SST forcing (solid red); and the constant circulation Ocean Circulation Inverse Model (dash black, DeVries et al. 2014) that imposes variable $pCO_2^{atmosphere}$. In B, dashed lines are correlated at 0.97-0.99 and the solid lines 0.92 (Table S4). In A, the mean flux of the observationally-based products is increased by 0.45 PgC/yr (Jacobson et al. 2007) to account for the outgassing of natural carbon supplied by rivers to the ocean.

610

Figure 2

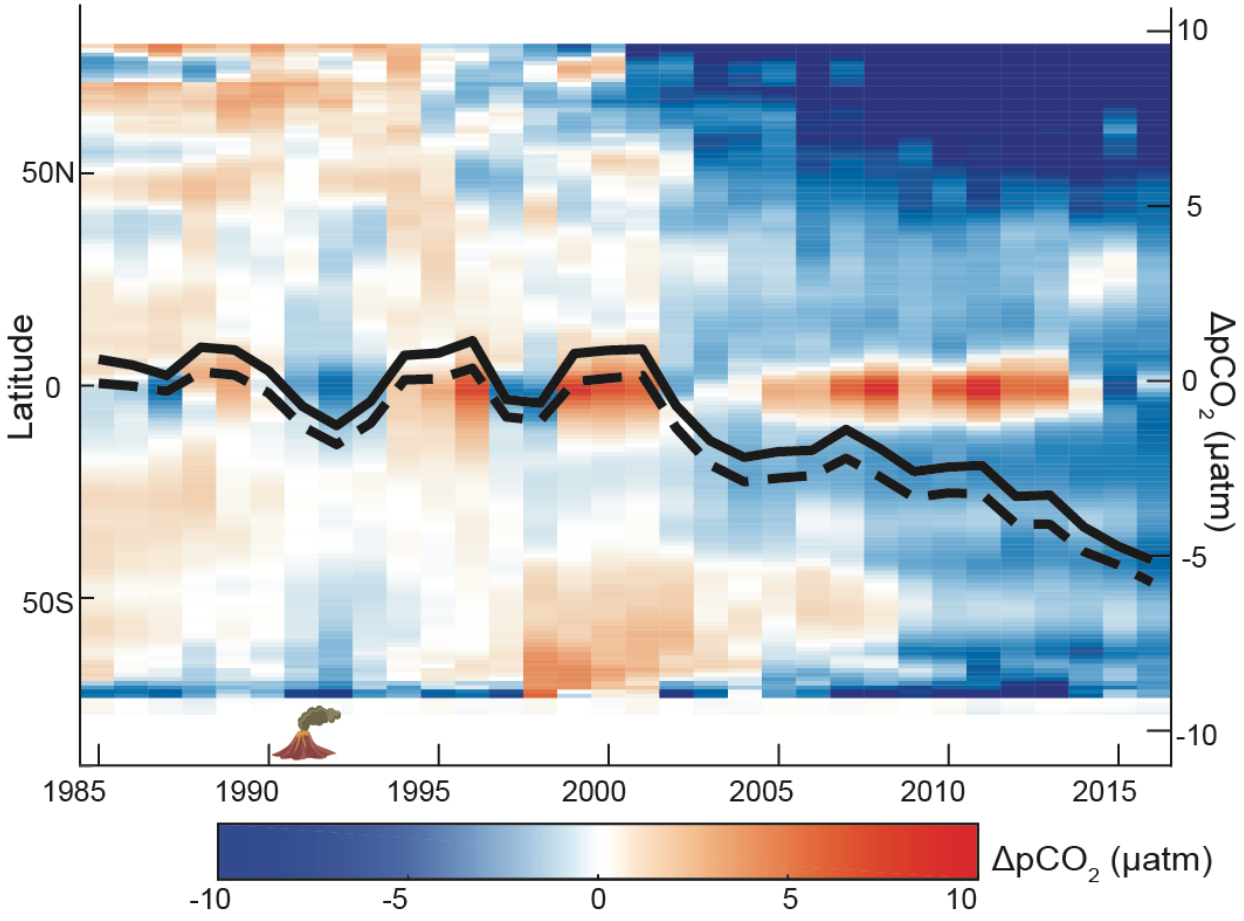

611

612 **Fig 2: Latitudinal mean anomaly ΔpCO_2** (µatm) from the ensemble mean of the
613 observationally-based products. Anomaly is calculated from the 1990-1999 mean. Annual
614 ΔpCO_2 time series overlaid in black for global (solid) and global excluding east equatorial
615 Pacific biome (dashed).
616

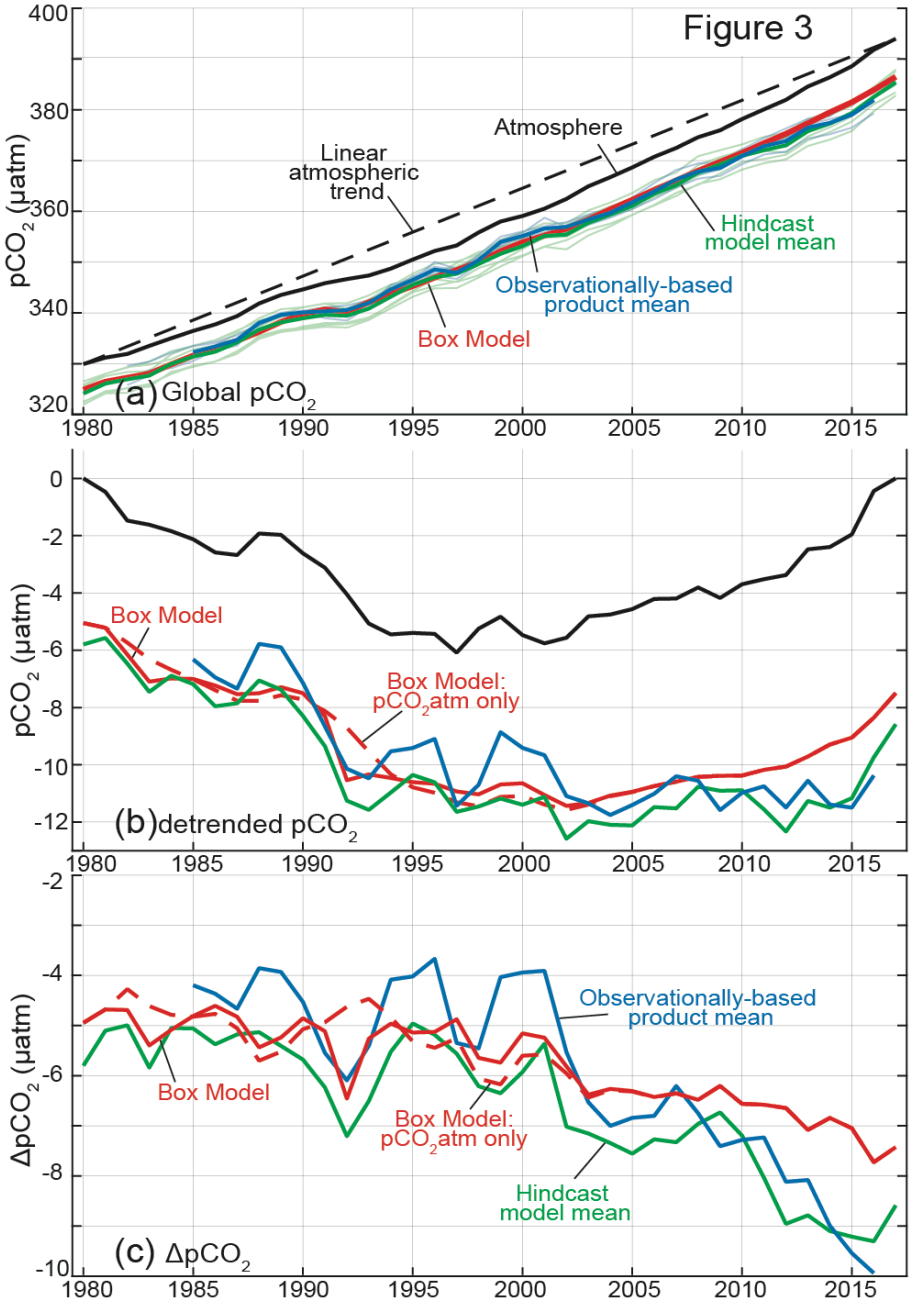

Fig 3: Trends of $pCO_2^{atmosphere}$ (black) and pCO_2^{ocean} (colors) (**A**) with trend, (**B**) detrended with the long-term $pCO_2^{atmosphere}$ trend (1.70 µatm/yr from 1980 to 2017), (**C**) ΔpCO_2 (= pCO_2^{ocean} - $pCO_2^{atmosphere}$). Observationally-based products mean (blue), hindcast model mean (green) and upper ocean diagnostic box model (red). The box model is forced with only $pCO_2^{atmosphere}$ (dashed) and with both $pCO_2^{atmosphere}$ and volcano-associated SST change (solid). Hindcast models without the water vapor correction applied to their atmospheric pCO_2 time series are corrected to account for that difference. Fig S6 expands on these results by including additional box model forcing scenarios.

Figure 4

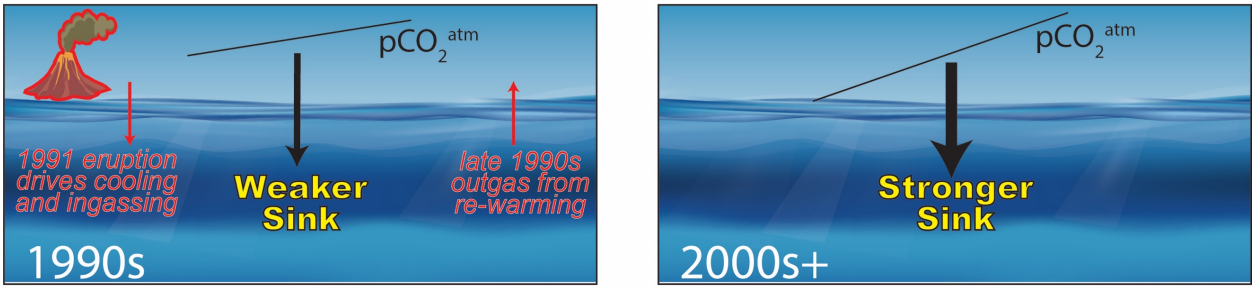

626

627 **Fig 4: Mechanisms of recent decadal variability of the ocean carbon sink**. (**A**) The reduced
628 sink of the 1990s (black arrow) was due to a slowing of the $pCO_2^{atmosphere}$ growth rate, and the
629 rapid cooling and slower warming recovery in response to the eruption of Mt. Pinatubo (red
630 arrows). (**B**) In the 2000s and beyond, $pCO_2^{atmosphere}$ growth accelerates, leading to enhanced
631 ΔpCO_2 and sink growth.

632

Supporting Information

External forcing explains recent decadal variability of the ocean carbon sink

Galen A. McKinley[1], Amanda R. Fay[1], Yassir A. Eddebbar[2], Lucas Gloege[1],
Nicole S. Lovenduski[3]

[1] Lamont Doherty Earth Observatory / Columbia University, Palisades NY
[2] Scripps Institution of Oceanography, La Jolla, CA
[3] University of Colorado at Boulder, Boulder, CO

Models and Products

In addition to the 6 hindcast models used throughout this analysis, nine (9) hindcast model-based estimates of the effect of constant climate and variable $pCO_2^{atmosphere}$ for 1980-2016 are used to provide a comparison to other recent work (Devries et al. 2019; Figure 1b). Of the 9 models in this suite, 6 are essentially the same as those in our primary analysis. Correlation of the mean of this 9-member ensemble with variable climate and variable $pCO_2^{atmosphere}$ for 1980-2016 (Devries et al. 2019) to our suite of hindcast models is 0.99, indicating that the results are interchangeable for the purpose of this paper.

Flux analysis

Individual models and products utilize different methods for flux calculation including wind speed products and parameterizations. References included in Table S1 and Table S2 provide details on each model and product.

pCO_2 analysis

For both models and products, maps of flux indicate that ice coverage has been considered in the calculation, however spatially-resolved pCO_2 do not indicate this masking. Therefore, we begin by accounting for ice coverage in the pCO_2 analysis for each model and product [$pCO_2^{ocean} = pCO_2^{ocean,\,raw} * (1\text{-ice fraction})$] with ice fraction product NOAA_OI_SST_V2. These data provided by the NOAA/OAR/ESRL PSD, Boulder, Colorado USA from their website at https://www.esrl.noaa.gov/psd/ (Reynolds et al., 2002). The ice fraction product begins in 1982. In order to apply it to models that begin in 1980, we use the 1982-1989 monthly climatology for 1980 and 1981.

ΔpCO_2 is calculated at annual timescales by [$\Delta pCO_2 = pCO_2^{ocean} - pCO_2^{atmosphere}$] where $pCO_2^{atmosphere}$ is the dry air mixing ratio of atmospheric CO_2 (xCO_2) from the ESRL surface marine boundary layer CO_2 product available at https://www.esrl.noaa.gov/gmd/ccgg/mbl/data.php (Dlugokencky et al., 2017) and sea level pressure (Kalnay et al., 1996) at monthly resolution. NCEP Reanalysis Derived data provided by the NOAA/OAR/ESRL PSD, Boulder, Colorado, USA, from their web site at https://www.esrl.noaa.gov/psd/. A global area-weighted annual time series is then calculated for $pCO_2^{atmosphere}$ before calculating ΔpCO_2.

Upper Ocean Box Model, Additional Discussion

The mean and standard deviation of the air-sea CO_2 flux in the box model is not very sensitive to reasonable parameter choices. Across the observed k_w range of 12-18 cm/hr (Wanninkhof, 2014), and reasonable estimates for the rate of overturning circulation (ν) from 15-35 Sv (DeVries et al., 2017), the mean flux is not sensitive (Fig S3a); instead ΔpCO_2 adjusts such that the flux drives surface ocean pCO_2 so that it can, on the long-term, rise at the same rate as $pCO_2^{atmosphere}$ (Fig S6). The depth of the box does impact the mean flux (Fig S3b,c) because this alters the total volume of low carbon water supplied from depth that needs to equilibrate toward the rising $pCO_2^{atmosphere}$. The magnitude of variability ranges by approximately 20% across k_w values, but is not sensitive

to ν. As the depth of the box becomes shallower than 400m, variability of the flux declines by up to 25%. This sensitivity analysis indicates that our parameter choices do not dramatically influence our results. In addition, our choice of parameters is supported by the fact that the box model forced with only $pCO_2^{atmosphere}$ can capture air-sea CO_2 flux variability that is essentially identical to the ensemble result from constant climate three-dimensional ocean models (Fig. 1b).

When the box model is forced with only the 1980-2017 linear change of $pCO_2^{atmosphere}$ (1.78 μatm/yr) (Fig S6a,d), the response is an increased carbon flux into the ocean until the point that a new approximately steady-state ΔpCO_2 is achieved (Fig S6e). This ΔpCO_2 provides sufficient flux for the annual growth of pCO_2^{ocean} to approximately match that of $pCO_2^{atmosphere}$, and thus there is a steady carbon flux (Fay & McKinley, 2013; McKinley et al., 2017). The timescale for this equilibration is approximately 10 years, calculated as 2 e-folding timescales for the adjustment to a new steady state for the box model forced only with linear trend of $pCO_2^{atmosphere}$. Because there are no short-term anomalies in either pCO_2^{ocean} or $pCO_2^{atmosphere}$ when forced with linear trend of $pCO_2^{atmosphere}$, there is also no interannual variability of ΔpCO_2 (Fig S6f) or flux (not shown) in this case. Adding the volcano SST forcing (Fig S2) the box model forced with linear trend of $pCO_2^{atmosphere}$, there are immediate negative anomalies in ΔpCO_2, indicating an increased sink, and then a relaxation as the surface ocean re-warms with the fading of the volcano cooling effect (Fig S6e,f).

Table S1: Hindcast model resolution and coverage period. Total ocean coverage is based on the 1°x1° mask of Gruber et al., 2009 used in the RECCAP project (Canadell et al., 2011).

Model Name ***Reference***	**Resolution** **Years**	**Area Coverage** **(% global ocean)**
MITgcm-REcoM2 *Hauck et al. 2018*	Monthly, 1°x1° 1958-2017	3.51e+14m^2 (96%)
NEMO-PlankTOM *Buitenhuis et al. 2010*	Monthly, 1°x1° 1959-2017	3.49e+14m^2 (96%)
CNRM-ESM2-1 *Séférian et al. 2016*	Monthly, 1°x1° 1848-2017	3.61e+14 m^2 (99%)
CCSM-BEC *Doney et al. 2009*	Monthly, 1°x1° 1958-2017	3.29e+14m^2 (90%)
MPI-ESM *Paulsen et al. 2017*	Monthly, 1°x1° 1959-2017	3.42e+14m^2 (94%)
NorESM-OCv1.2 *Schwinger et al. 2016*	Monthly, 1°x1° 1948-2017	3.70e+14m^2 (101%)

Table S2: Observationally-based product resolution and coverage period. In the case of time-varying coverage masks, area coverage listed is for a most conservative mask which requires a value for every month of the time period. In some cases, this differs for flux and pCO_2 variables. Total ocean coverage is based on the 1x1° mask of Gruber et al., 2009 used in the RECCAP project (Canadell et al., 2011).

Product Name ***Reference***	**Resolution Years**	**Area Coverage (% global ocean)**	**Mean Correction to Flux (to pCO_2)** (section 2.4)
LSCE *Denvil-Sommer et al. 2019*	Monthly, 1°x1° 1985-2016	2.93e+14m^2 (80%)	0.41 $PgCyr^{-1}$ (3.18µatm)
CSIR-ML6 *Gregor et al. 2019*	Monthly, 1°x1° 1982-2016	Flux: 3.11e+14m^2 (85%) pCO_2: 3.13e+14 (86%)	0.30 $PgCyr^{-1}$ (1.98µatm)
SOM-FFN *Landschützer et al. 2017*	Monthly, 1°x1° 1982-2018	3.19e+14m^2 (87%)	0.25 $PgCyr^{-1}$ (1.56µatm)
Jena-MLS *Rödenbeck et al. 2013*	Monthly, 5°x5° 1982-2018 flux	3.67e+14m^2 (100%)	0

Table S3: Parameters and values for the upper ocean diagnostic box model

Parameter	Value	References / Notes
ν	25 Sv	Devries et al. 2017
DIC_{deep}	2055 mmol/m^3	Sarmiento and Gruber, 2006
k_w	15 cm/hr	Wanninkhof, 2014
Temperature	18^{o}C	Sarmiento and Gruber, 2006
Salinity	35psu	
Alkalinity	2350 mmol/m^3	Sarmiento and Gruber, 2006
dz	500m	
Global ocean area (A)	3.34e14 m^2	96% of global ocean

Table S4: Correlation of air-sea carbon flux for hindcast models, observationally-based products, and box model runs as shown in Figure 1. Detrended timeseries correlations shown in parenthesis. Correlations are shown for longest overlapping timeseries. Correlations in bold are significant at $p<0.05$.

	Hindcast models 1980-2017	Box Model 1980-2017	Hindcast models: pCO_2^{atm} only 1980-2016	Box Model: pCO_2^{atm} only 1980-2017	OCIM: pCO_2^{atm} only 1980-2017
Observationally-based products 1985-2016	**0.95 (0.78)**	**0.94 (0.79)**	**0.86** (0.15)	**0.82** (0.17)	**0.87** (0.24)
Hindcast models 1980-2017	**1**	**0.92 (0.64)**	**0.89** (-0.01)	**0.86** (0.02)	**0.90** (-0.01)
Box Model 1980-2017	**-**	**1**	**0.88 (0.36)**	**0.90 (0.46)**	**0.90 (0.43)**
Hindcast models: pCO_2^{atm} only 1980-2016	**-**	**-**	**1**	**0.98 (0.93)**	**0.99 (0.96)**
Box Model: pCO_2^{atm} only 1980-2017	**-**	**-**	**-**	**1**	**0.98 (0.85)**

Table S5: Global Mean Fluxes (PgC/yr) by decade. Observationally-based products have been masked to account for missing ocean area.

Global Mean Flux (PgC/yr)	1980-1989	1990-1999	2000-2009	2010-2017
Box Model: actual pCO_2^{atm} and volcano	-1.85	-1.97	-2.11	-2.48
Box Model: actual pCO_2^{atm}	-1.79	-1.88	-2.23	-2.50
Box Model: volcano only	-2.03	-2.31	-2.13	-2.20
Box Model: linear pCO_2^{atm}	-1.97	-2.22	-2.24	-2.22
Hindcast model mean	-1.68	-1.90	-2.05	-2.37
Observationally-based product mean	-1.42[a]	-1.62	-1.79	-2.38[b]

a. 3 observationally-based products begin in 1982 and 1 in 1985 (Table S2)
b. Observationally-based products through 2016 only

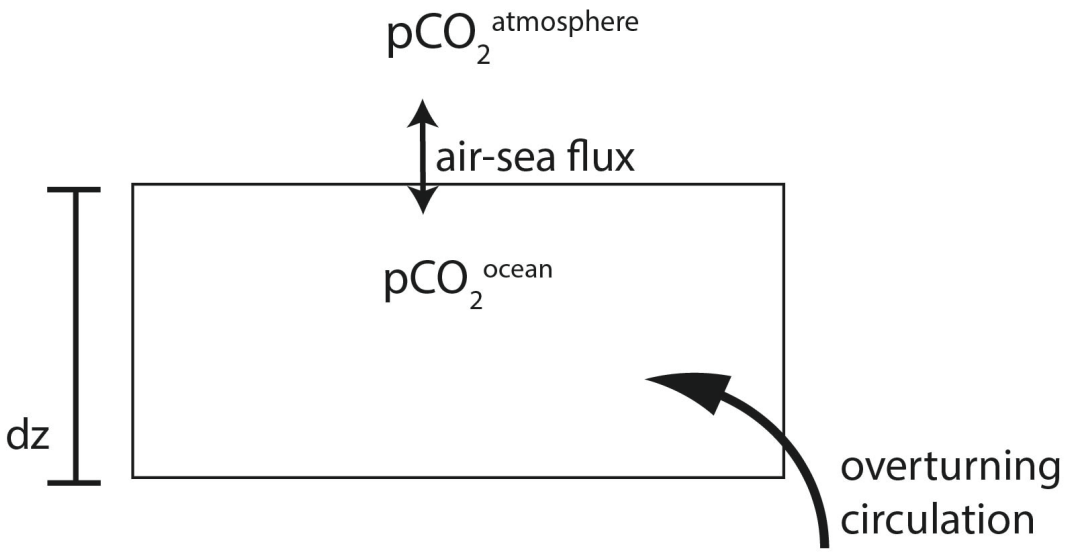

Figure S1: Schematic of the single-reservoir upper ocean diagnostic box model

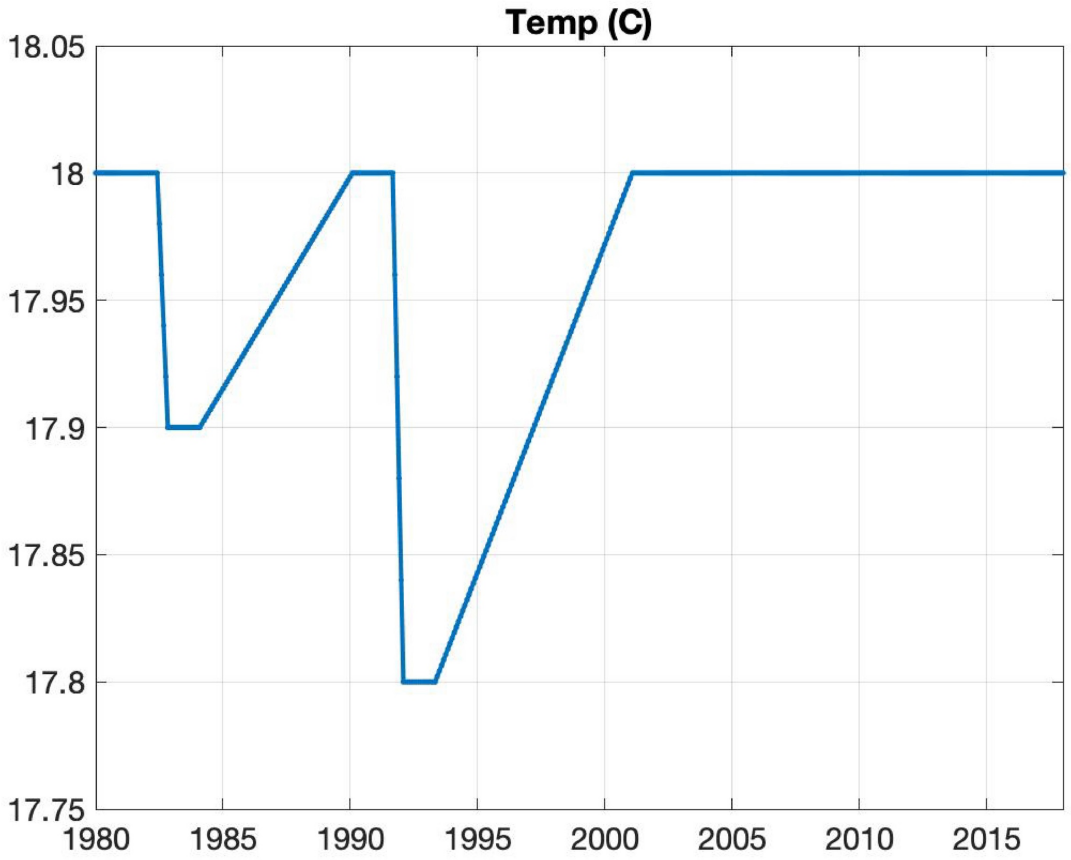

Figure S2: Sea surface temperature forcing for box model. Idealized SST response, based on two earth system models forced response to El Chichon and Mt. Pinatubo (Eddebbar et al. 2019, their Figure 1a)

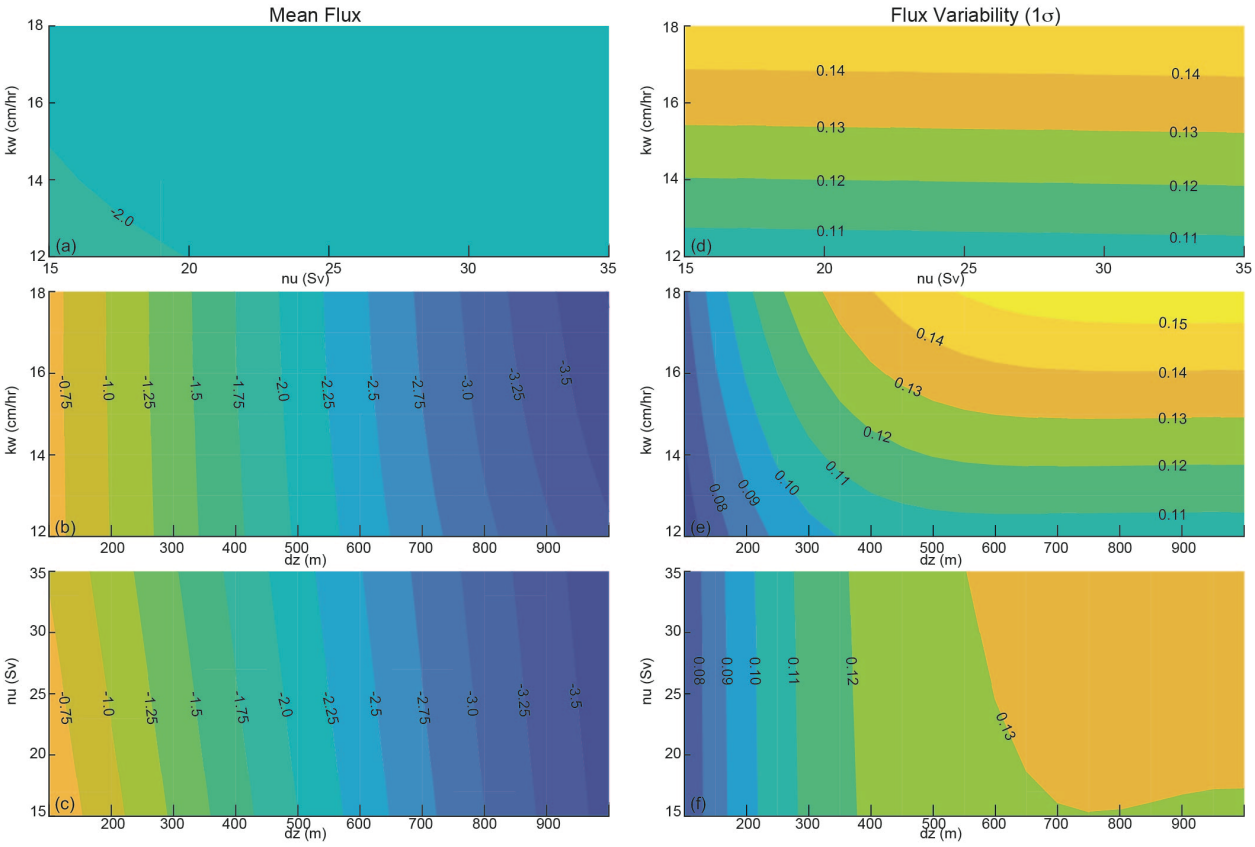

Figure S3: Sensitivity of the air-sea flux (PgC/yr) on the mean (a-c) and for variability (d-f) in the box model. The impact of varying values of piston velocity (k_w), the rate of the overturning circulation (ν), and the depth of the box (dz) on the box model forced with both $pCO_2^{atmosphere}$ and the SST response to volcanos. Default values are used for the third parameter in each case, e.g. (a,d) dz = 500m; (b,e), ν = 25 Sv; (c,f) k_w = 15 cm/hr.

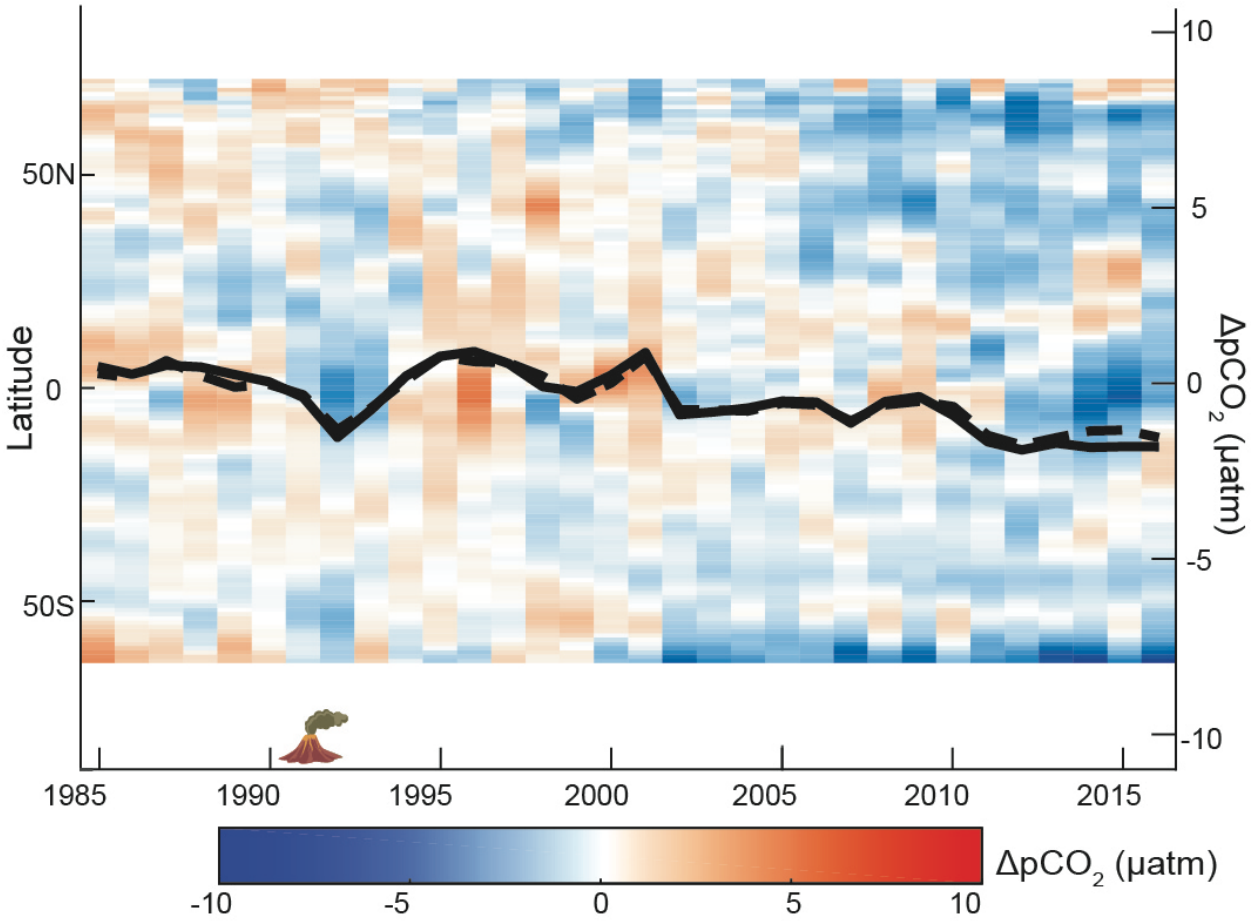

Figure S4: Latitudinal mean anomaly ΔpCO_2 (µatm) from the ensemble mean of the hindcast models. Anomaly is calculated from the 1990-1999 mean. Latitudes with >50% mean ice coverage omitted. Annual ΔpCO_2 time series overlaid in black for global (solid) and global excluding east equatorial Pacific biome (dashed).

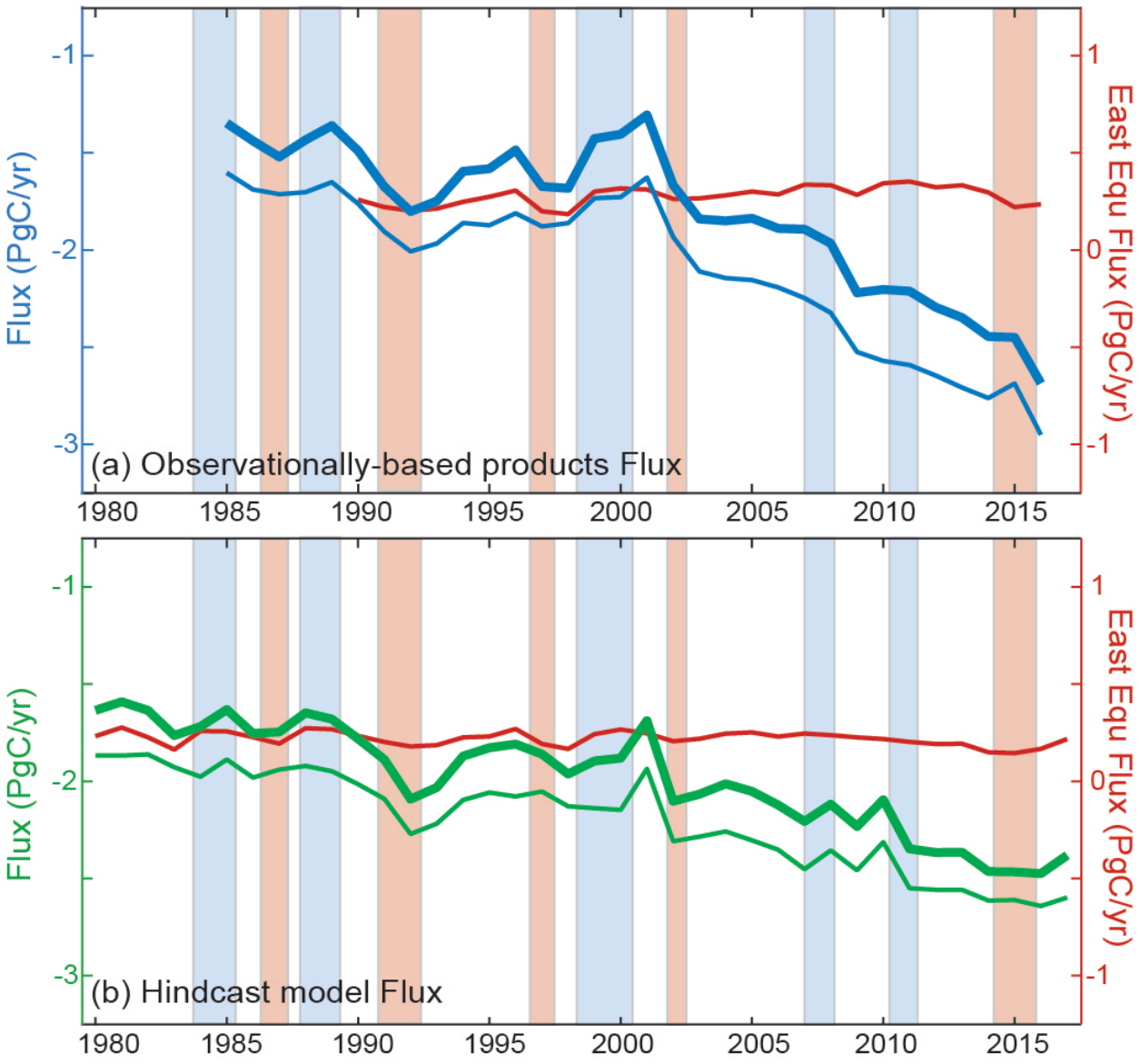

Figure S5: Comparison of global fluxes and fluxes for the globe without the eastern equatorial Pacific (Fay & McKinley 2014). (A) Observationally-based products (blue), (B) hindcast models (green) for global (thick line), global without eastern equatorial Pacific biome (thin line), and only east equatorial Pacific biome (red line). Shaded bars represent ENSO events; blue for La Niña, red for El Niño. Though there is a high inverse correlation between CO_2 fluxes and the Nino 3.4 index in the eastern equatorial Pacific (r = -0.63 for both products and models), this region is small (4% of the global ocean area) and is not dominant to the global decadal flux variability.

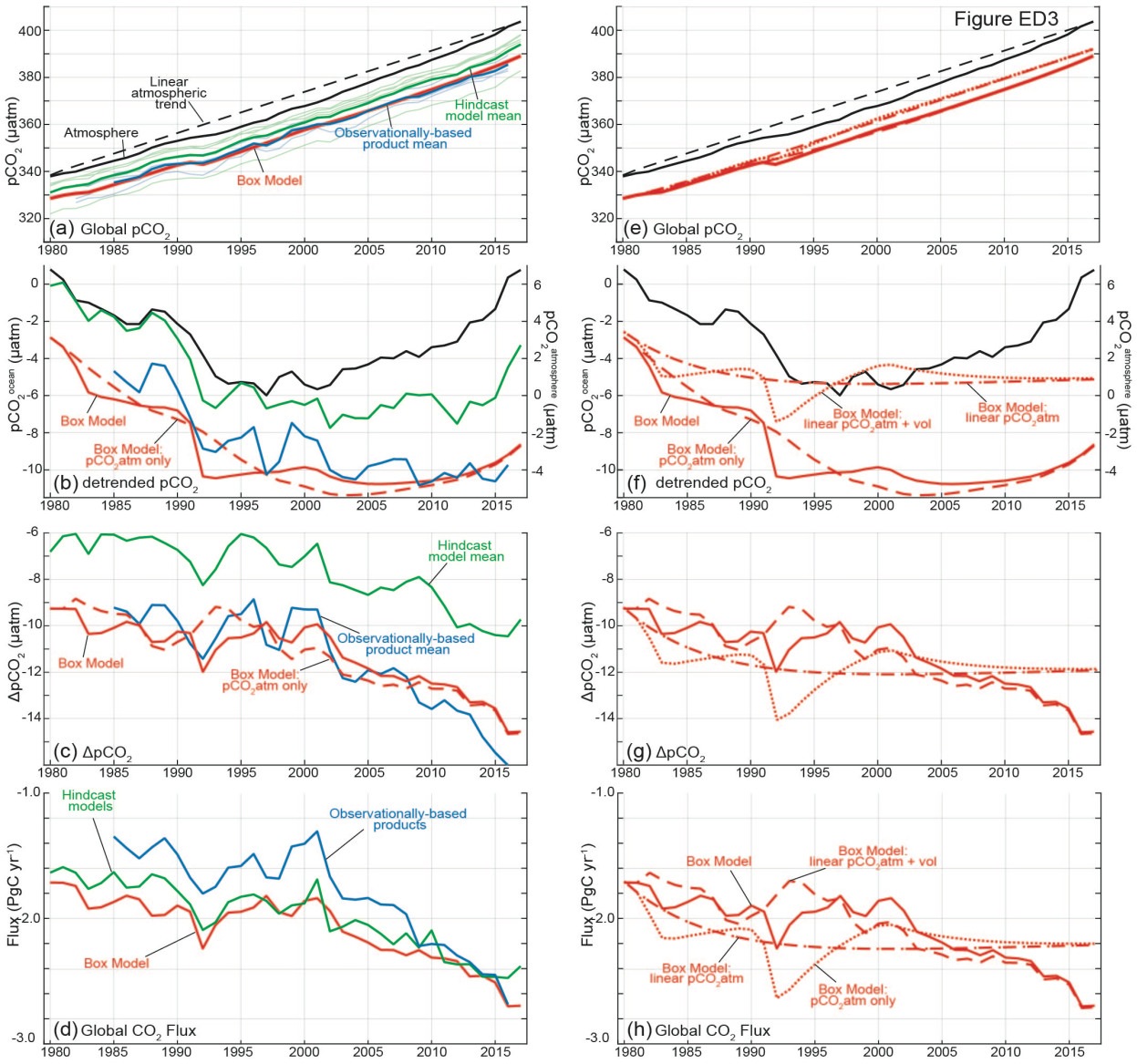

Figure S6: Trends of $pCO_2^{atmosphere}$, pCO_2^{ocean}, and Air-sea CO_2 flux (**A**) with trend, (**B**) detrended with the long-change in $pCO_2^{atmosphere}$ (1.78 µatm/yr from 1980 to 2017), (**C**) ΔpCO_2 (= pCO_2^{ocean} - $pCO_2^{atmosphere}$), and (**D**) global flux. Observationally-based products (blue), hindcast models (green), upper ocean diagnostic box model (red). (**E**) Box model, 4 versions with trend, (**F**) detrended with the long-term $pCO_2^{atmosphere}$ change (1.78 µatm/yr), (**G**) ΔpCO_2 (= pCO_2^{ocean} - $pCO_2^{atmosphere}$), and (**H**) global flux. E-H, the box model forced only with the linear $pCO_2^{atmosphere}$ trend (dot-dash); with both linear $pCO_2^{atmosphere}$ trend and volcano SST (dotted); with observed $pCO_2^{atmosphere}$ only (dash); and with observed $pCO_2^{atmosphere}$ and volcano SST (solid).

Supporting Information

External forcing explains recent decadal variability of the ocean carbon sink

Galen A. McKinley[1], Amanda R. Fay[1], Yassir A. Eddebbar[2], Lucas Gloege[1],
Nicole S. Lovenduski[3]

[1] Lamont Doherty Earth Observatory / Columbia University, Palisades NY
[2] Scripps Institution of Oceanography, La Jolla, CA
[3] University of Colorado at Boulder, Boulder, CO

Models and Products

In addition to the 6 hindcast models used throughout this analysis, nine (9) hindcast model-based estimates of the effect of constant climate and variable $pCO_2^{atmosphere}$ for 1980-2016 are used to provide a comparison to other recent work (Devries et al. 2019; Figure 1b). Of the 9 models in this suite, 6 are essentially the same as those in our primary analysis. Correlation of the mean of this 9-member ensemble with variable climate and variable $pCO_2^{atmosphere}$ for 1980-2016 (Devries et al. 2019) to our suite of hindcast models is 0.99, indicating that the results are interchangeable for the purpose of this paper.

Flux analysis

Individual models and products utilize different methods for flux calculation including wind speed products and parameterizations. References included in Table S1 and Table S2 provide details on each model and product.

pCO_2 analysis

For both models and products, maps of flux indicate that ice coverage has been considered in the calculation, however spatially-resolved pCO_2 do not indicate this masking. Therefore, we begin by accounting for ice coverage in the pCO_2 analysis for each model and product [$pCO_2^{ocean} = pCO_2^{ocean,\,raw}$ *(1-ice fraction)] with ice fraction product NOAA_OI_SST_V2. These data provided by the NOAA/OAR/ESRL PSD, Boulder, Colorado USA from their website at https://www.esrl.noaa.gov/psd/ (Reynolds et al., 2002). The ice fraction product begins in 1982. In order to apply it to models that begin in 1980, we use the 1982-1989 monthly climatology for 1980 and 1981.

ΔpCO_2 is calculated at annual timescales by [$\Delta pCO_2 = pCO_2^{ocean} - pCO_2^{atmosphere}$] where $pCO_2^{atmosphere}$ is the dry air mixing ratio of atmospheric CO_2 (xCO_2) from the ESRL surface marine boundary layer CO_2 product available at https://www.esrl.noaa.gov/gmd/ccgg/mbl/data.php (Dlugokencky et al., 2017) multiplied by sea level pressure (Kalnay et al., 1996) at monthly resolution, taking into account the water vapor correction according to Dickson et al. (2007). NCEP Reanalysis Derived data provided by the NOAA/OAR/ESRL PSD, Boulder, Colorado, USA, from their web site at https://www.esrl.noaa.gov/psd/. A global area-weighted annual time series is then calculated for $pCO_2^{atmosphere}$ before calculating ΔpCO_2 for each model and product. Only the CNRM model accounted for water vapor pressure at the time it was run. For pCO_2 to be plotted consistently with CNRM and the observationally based products, we must apply an adjustment to the remaining models that do not include the water vapor correction. To do so, we offset their global mean pCO_2 time series by the difference between the observed $pCO_2^{atmosphere}$ calculated with and without the water vapor correction. This correction averages 9.2 µatm over years 1980-2017.

Upper Ocean Box Model, Additional Discussion

For the box model, the temperature is set at 14C, consistent with the observed SST global mean outside 15S-15N. The piston velocity of k_w = 25 cm/hr is higher than the global mean of

approximately 17 cm/hr (Wanninkhof, 2014; Neagler et al. 2006). This choice is justified by the lack of spatial variability in ΔpCO_2 and in piston velocity, normally parameterized as a square function of windspeed (Wanninkhof, 2014). Larger ΔpCO_2 are coincident at higher latitudes with stronger winds, and thus with larger piston velocities (Takahashi et al. 2009). Since the product of the global mean will naturally be less than the mean of the product when extreme values are correlated, a higher piston velocity is selected to allow for a reasonable ΔpCO_2 and air-sea CO_2 flux to co-exist in the box model.

The mean and standard deviation of the air-sea CO_2 flux in the box model is not very sensitive to reasonable parameter choices. Across the observed k_w range of 15-30 cm/hr (Wanninkhof, 2014), and reasonable estimates for the rate of overturning circulation (ν) from 40-80 Sv (DeVries et al., 2017), the mean flux is not sensitive, only varying by 0.5PgC/yr (Fig S3a). The depth of the box does impact the mean flux (Fig S3b,c) because these alter the volume and rate of supply of low carbon water from depth that must equilibrate with rising $pCO_2^{atmosphere}$. The magnitude of variability ranges by approximately 20% across k_w values, but is not sensitive to ν (Fig S3d). This sensitivity analysis indicates that our parameter choices do not dramatically influence our key result with respect to the magnitude and pattern of variability. In addition, our choice of parameters is supported by the fact that the box model forced with only $pCO_2^{atmosphere}$ can capture air-sea CO_2 flux variability that is essentially identical to the ensemble result from constant climate three-dimensional ocean models (Fig. 1b).

When the box model is forced with only the 1980-2017 linear change of $pCO_2^{atmosphere}$ (1.70 μatm/yr) (Fig S6a,d), there is a steadily growing carbon flux into the ocean in response to the growing $pCO_2^{atmosphere}$ (Fig S6e). The continued irrigation of the near-surface ocean with low DIC waters allows for continued growth of ΔpCO_2, consistent with the global long-term increasingly negative ΔpCO_2 (Fig. 2, McKinley et al. 2017). Because there are no short-term anomalies in either pCO_2^{ocean} or $pCO_2^{atmosphere}$ when forced with linear trend of $pCO_2^{atmosphere}$, there is also no interannual variability of ΔpCO_2 (Fig S6f) or flux (Fig S6h) in this case. Adding the volcano SST forcing (Fig S2) to the box model forced with linear $pCO_2^{atmosphere}$, there are immediate negative anomalies in ΔpCO_2, indicating an increased sink, and then a relaxation as the surface ocean re-warms with the fading of the volcano cooling effect (Fig S6e,f).

Table S1: Hindcast model resolution and coverage period. Total ocean coverage is based on the 1°x1° mask of Gruber et al., 2009 used in the RECCAP project (Canadell et al., 2011).

Model Name ***Reference***	**Resolution** **Years**	**Area Coverage** **(% global ocean)**
MITgcm-REcoM2 *Hauck et al. 2018*	Monthly, 1°x1° 1958-2017	3.51e+14m^2 (96%)
NEMO-PlankTOM *Buitenhuis et al. 2010*	Monthly, 1°x1° 1959-2017	3.49e+14m^2 (96%)
CNRM-ESM2-1 *Séférian et al. 2016*	Monthly, 1°x1° 1848-2017	3.61e+14 m^2 (99%)
CCSM-BEC *Doney et al. 2009*	Monthly, 1°x1° 1958-2017	3.29e+14m^2 (90%)
MPI-ESM *Paulsen et al. 2017*	Monthly, 1°x1° 1959-2017	3.42e+14m^2 (94%)
NorESM-OCv1.2 *Schwinger et al. 2016*	Monthly, 1°x1° 1948-2017	3.70e+14m^2 (101%)

Table S2: Observationally-based product resolution and coverage period. In the case of time-varying coverage masks, area coverage listed is for a most conservative mask which requires a value for every month of the time period. In some cases, this differs for flux and pCO_2 variables. Total ocean coverage is based on the 1x1° mask of Gruber et al., 2009 used in the RECCAP project (Canadell et al., 2011).

Product Name ***Reference***	**Resolution Years**	**Area Coverage (% global ocean)**	**Mean Correction to Flux (to pCO_2)** (section 2.4)
LSCE *Denvil-Sommer et al. 2019*	Monthly, 1°x1° 1985-2016	2.93e+14m^2 (80%)	0.41 $PgCyr^{-1}$ (3.16µatm)
CSIR-ML6 *Gregor et al. 2019*	Monthly, 1°x1° 1982-2016	Flux: 3.11e+14m^2 (85%) pCO_2: 3.13e+14 (86%)	0.33 $PgCyr^{-1}$ (2.46µatm)
SOM-FFN *Landschützer et al. 2017*	Monthly, 1°x1° 1982-2018	3.19e+14m^2 (87%)	0.25 $PgCyr^{-1}$ (1.55µatm)
Jena-MLS *Rödenbeck et al. 2013*	Monthly, 5°x5° 1982-2018 flux	3.67e+14m^2 (100%)	0

Table S3: Parameters and values for the upper ocean diagnostic box model

Parameter	Value	References / Notes
ν	60 Sv	Devries et al. 2017
DIC_{deep}	2055 mmol/m^3	Sarmiento and Gruber, 2006
k_w	25 cm/hr	Wanninkhof, 2014
Temperature	14^{o}C	
Salinity	35psu	
Alkalinity	2350 mmol/m^3	Sarmiento and Gruber, 2006
dz	200m	
Global ocean area (A)	3.34e14 m^2	96% of global ocean

Table S4: Correlation of air-sea carbon flux for hindcast models, observationally-based products, and box model runs as shown in Figure 1. Detrended timeseries correlations shown in parenthesis. Correlations are shown for longest overlapping timeseries. Correlations in bold are significant at $p<0.05$.

	Hindcast models 1980-2017	Box Model 1980-2017	Hindcast models: pCO_2^{atm} only 1980-2016	Box Model: pCO_2^{atm} only 1980-2017	OCIM: pCO_2^{atm} only 1980-2017
Observationally-based products 1985-2016	**0.95 (0.78)**	**0.89 (0.54)**	**0.86** (0.15)	**0.82** (0.17)	**0.87** (0.24)
Hindcast models 1980-2017	**1**	**0.92 (0.57)**	**0.89** (-0.01)	**0.86** (0.02)	**0.90** (-0.01)
Box Model 1980-2017	**-**	**1**	**0.91 (0.49)**	**0.89 (0.41)**	**0.91 (0.50)**
Hindcast models: pCO_2^{atm} only 1980-2016	**-**	**-**	**1**	**0.974)**	**0.99 (0.96)**
Box Model: pCO_2^{atm} only 1980-2017	**-**	**-**	**-**	**1**	**0.98 (0.91)**

Table S5: Global Mean Fluxes (PgC/yr) by decade. Observationally-based products have been masked to account for missing ocean area.

Global Mean Flux (PgC/yr)	1980-1989	1990-1999	2000-2009	2010-2017
Box Model: actual pCO_2^{atm} and volcano	-1.73	-1.86	-2.11	-2.43
Box Model: actual pCO_2^{atm}	-1.71	-1.82	-2.15	-2.43
Box Model: volcano only	-1.84	-2.03	-2.11	-2.20
Box Model: linear pCO_2^{atm}	-1.82	-1.99	-2. 15	-2.28
Hindcast model mean	-1.68	-1.90	-2.05	-2.37
Observationally-based product mean[a]	-1.87[b]	-2.07	-2.24	-2.86[c]

a. The mean flux of the observationally-based products is increased by 0.45 PgC/yr (Jacobson et al. 2007) to account for background outgassing of riverine carbon.
b. 3 observationally-based products begin in 1982 and 1 in 1985 (Table S2)
c. Observationally-based products through 2016 only

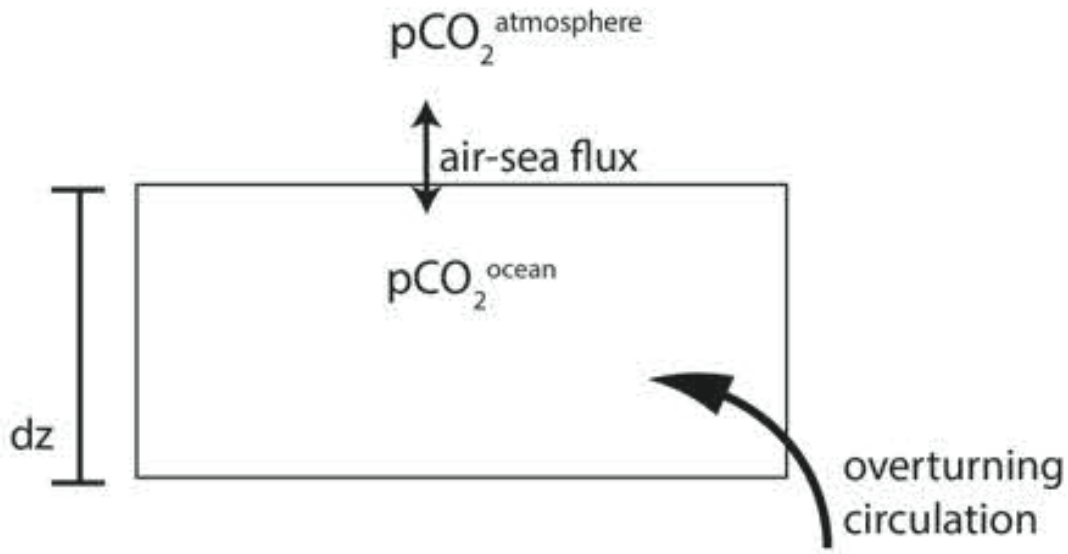

Figure S1: Schematic of the single-reservoir upper ocean diagnostic box model

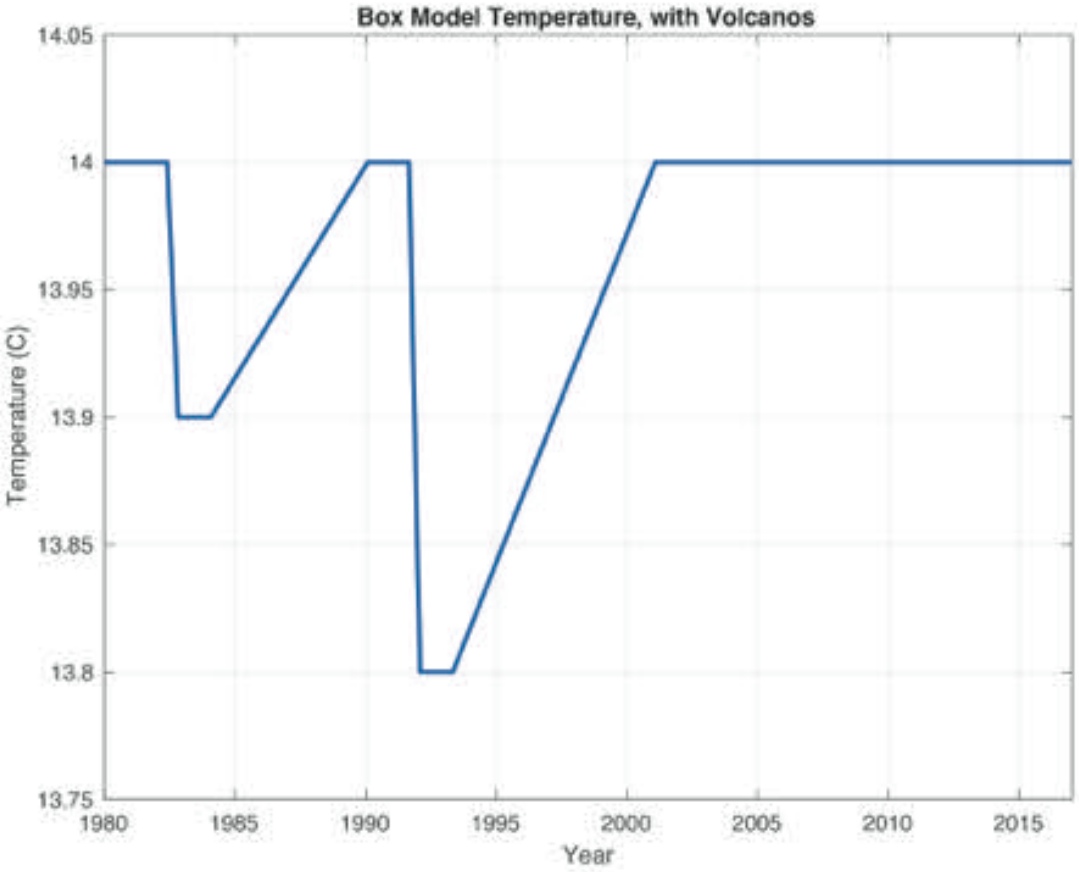

Figure S2: Sea surface temperature forcing for box model. Idealized SST response, based on two earth system models forced response to El Chichon and Mt. Pinatubo (Eddebbar et al. 2019, their Figure 1a)

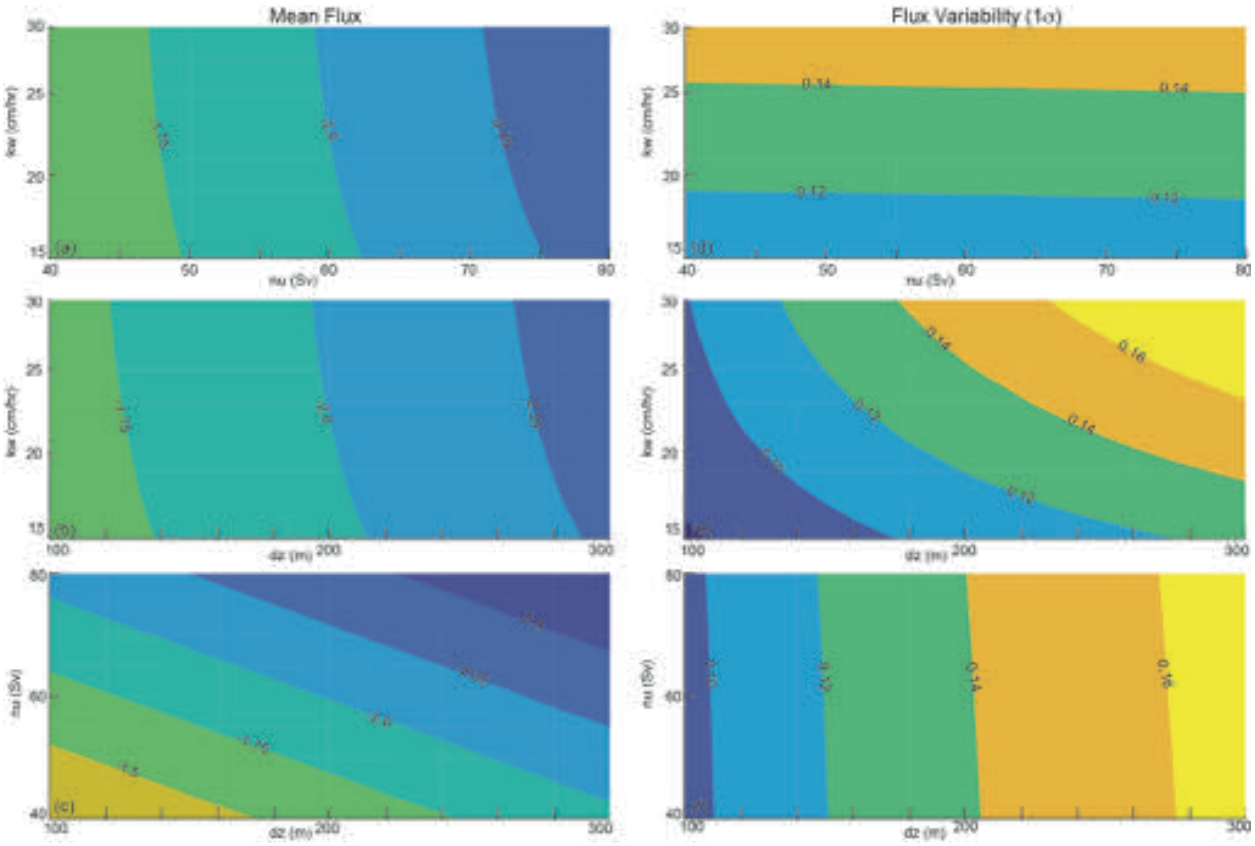

Figure S3: Sensitivity of the air-sea flux (PgC/yr) on the mean (a-c) and for variability (d-f) in the box model. The impact of varying values of piston velocity (k_w), the rate of the overturning circulation (ν), and the depth of the box (dz) on the box model forced with both $pCO_2^{atmosphere}$ and the SST response to volcanos. Default values are used for the third parameter in each case, e.g. (a,d) dz = 200m; (b,e), ν = 60 Sv; (c,f) k_w = 25 cm/hr.

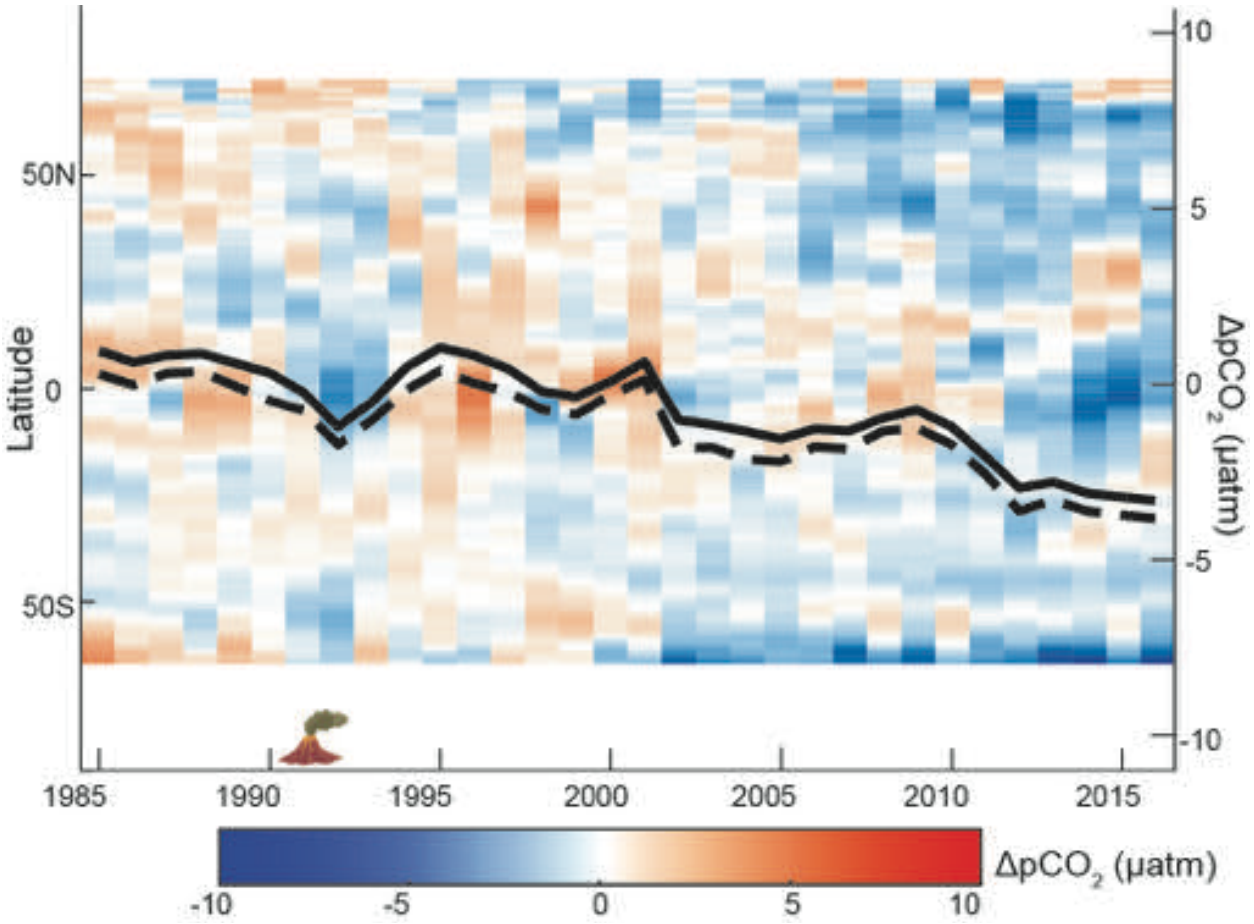

Figure S4: Latitudinal mean anomaly ΔpCO_2 (μatm) from the ensemble mean of the hindcast models. Anomaly is calculated from the 1990-1999 mean. Latitudes with >50% mean ice coverage omitted. Annual ΔpCO_2 time series overlaid in black for global (solid) and global excluding east equatorial Pacific biome (dashed).

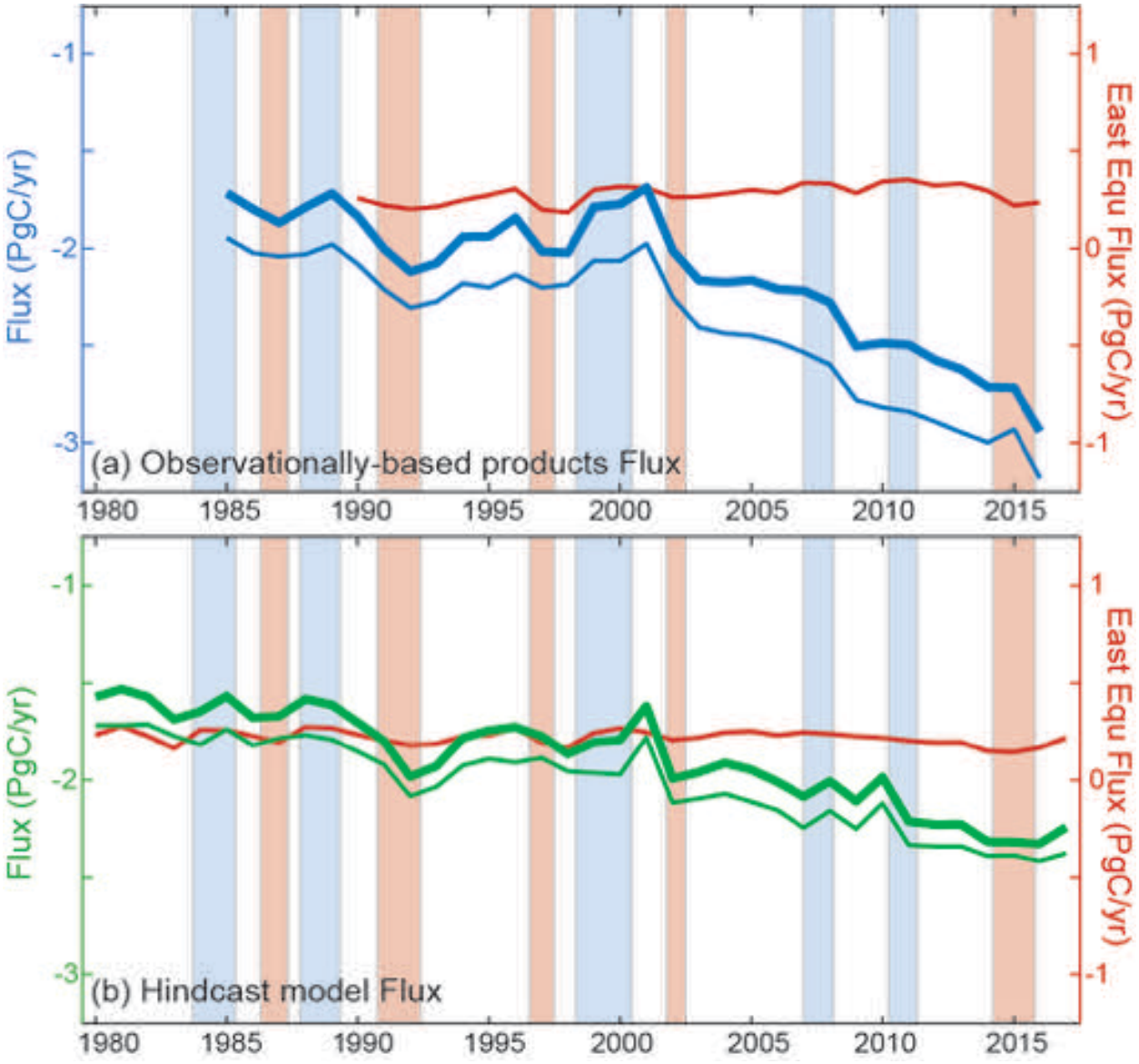

Figure S5: Comparison of global fluxes and fluxes for the globe without the eastern equatorial Pacific (Fay & McKinley 2014). (A) Observationally-based products (blue), (B) hindcast models (green) for global (thick line), global without eastern equatorial Pacific biome (thin line), and only east equatorial Pacific biome (red line). Shaded bars represent ENSO events; blue for La Niña, red for El Niño. Though there is a high inverse correlation between CO_2 fluxes and the Nino 3.4 index in the eastern equatorial Pacific (r = -0.72 for products and r = -0.63 for models), this region is small (4% of the global ocean area) and is not dominant to the global decadal flux variability. Observationally-based product fluxes include 0.45PgC/yr riverine efflux correction.

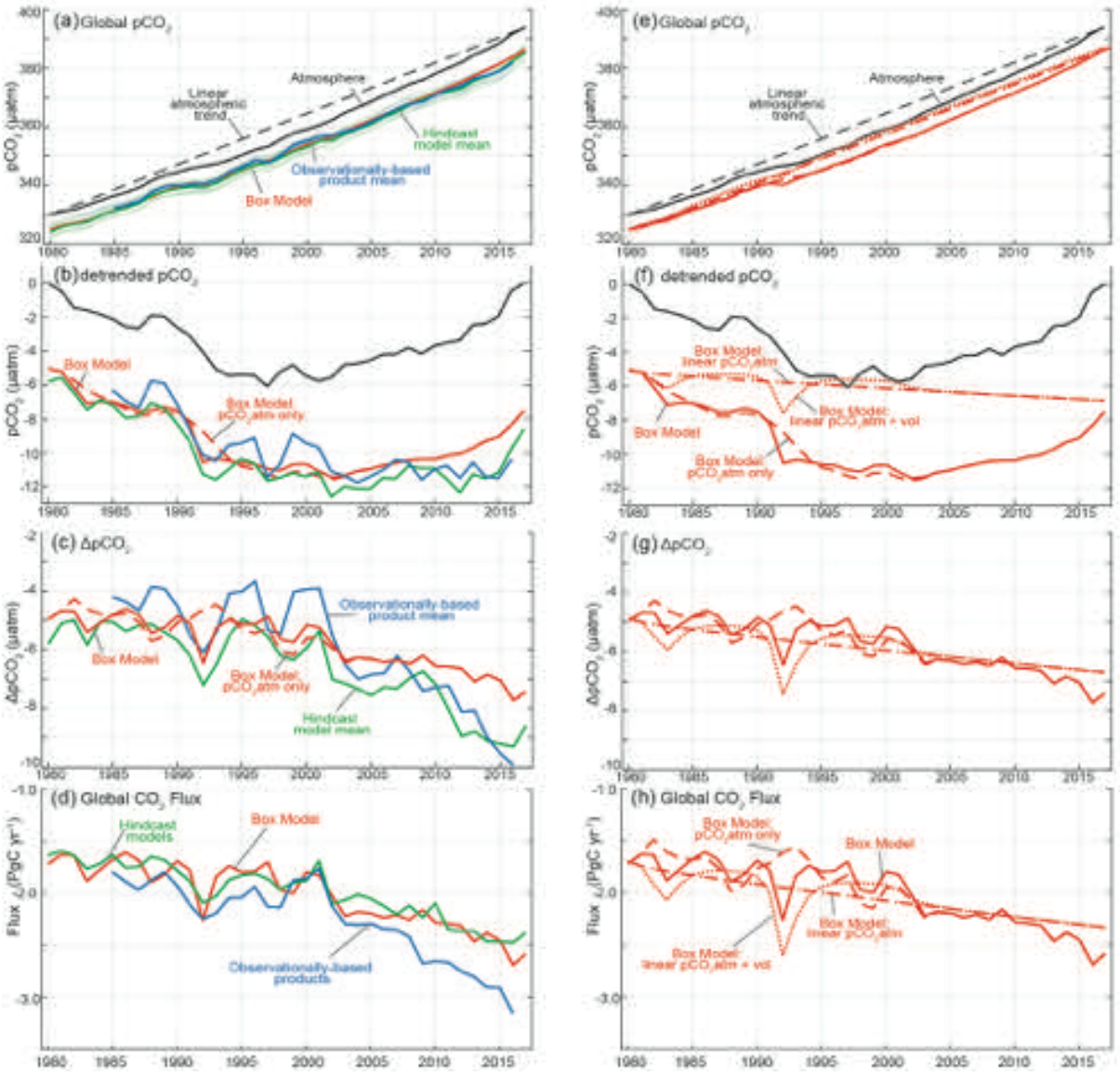

Figure S6: Trends of $pCO_2^{atmosphere}$, pCO_2^{ocean}, and Air-sea CO_2 flux (**A**) with trend, (**B**) detrended with the long-change in $pCO_2^{atmosphere}$ (1.70 µatm/yr from 1980 to 2017), (**C**) ΔpCO_2 (= pCO_2^{ocean} - $pCO_2^{atmosphere}$), and (**D**) global flux (as in Figure 1a). Observationally-based products (blue), hindcast models (green), upper ocean diagnostic box model (red). Hindcast models without the water vapor correction applied to their atmospheric pCO_2 time series are corrected to account for that difference. (**E**) Box model, 4 versions with trend, (**F**) detrended with the long-term $pCO_2^{atmosphere}$ change (1.70 µatm/yr), (**G**) ΔpCO_2 (= pCO_2^{ocean} - $pCO_2^{atmosphere}$), and (**H**) global flux. E-H, the box model forced only with the linear $pCO_2^{atmosphere}$ trend (dot-dash); with both linear $pCO_2^{atmosphere}$ trend and volcano SST (dotted); with observed $pCO_2^{atmosphere}$ only (dash); and with observed $pCO_2^{atmosphere}$ and volcano SST (solid).